



Gamma-Rays Induced Synthesis of Ag-Decorated ZnCo₂O₄–MoS₂ Heterostructure as Novel Photocatalyst and Effective Antimicrobial Agent for Wastewater Treatment Application

M. I. A. Abdel Maksoud¹ · Gharieb S. El-Sayyad² · Nahla Mamdouh³ · Waleed M. A. El Rouby³

Received: 17 February 2022 / Accepted: 14 May 2022 / Published online: 12 June 2022
© The Author(s) 2022

Abstract

The development of novel semiconductors-based-photocatalysts is a promising strategy for addressing environmental pollution. In the present study, gamma irradiation was utilized to induce the synthesis of the exceptionally efficient Ag-decorated ZnCo₂O₄–MoS₂ heterostructure. XRD and EDX analyses were verified the successful synthesis of Ag-decorated ZnCo₂O₄–MoS₂ heterostructure. Also, SEM and HR-TEM images were illustrated the heterostructure nature of the synthesized photocatalyst in the nanoscale regime. The obtained optical bandgap values verified that photocatalyst possesses a narrow semiconductor bandgap. Further, the Ag-decorated ZnCo₂O₄–MoS₂ heterostructure exhibited superior photodegradation potential towards MB (95.4% removal of the MB). The antimicrobial potency of the synthesized samples had been investigated through ZOI, MIC, growth curve assay, and the effect of UV illumination. Also, the antibiofilm behaviour has been studied. The antibacterial reaction mechanism had been estimated by membrane leakage assay and SEM imaging. The tested samples displayed a positive potency to a broad spectrum of bacteria like *Proteus mirabilis*, *Staphylococcus aureus*, *Pseudomonas aeruginosa*, and *Candida albicans*. In particular, Ag–MoS₂–ZnCo₂O₄ nanocomposite possessed the highest impact, followed by the spinal ZnCo₂O₄ NPs towards all the tested pathogenic microbes. In this assessment, the Ag-decorated ZnCo₂O₄–MoS₂ heterostructure has been shown to be a promising candidate for wastewater treatment application.

Keywords Gamma- radiation · Zinc cobaltite · Molybdenum disulfide · Antimicrobial activity · Wastewater treatment

M. I. A. Abdel Maksoud and Gharieb S. El-Sayyad have equal contribution.

✉ M. I. A. Abdel Maksoud
muhamadmqsod@gmail.com;
muhamad.abdelmaksoud@eaea.org.eg

✉ Gharieb S. El-Sayyad
Gharieb.Elsayyad2017@gmail.com;
Gharieb.S.Elsayyad@eaea.org.eg

¹ Radiation Physics Department, National Center for Radiation Research and Technology (NCRRT), Egyptian Atomic Energy Authority (EAEA), Cairo, Egypt

² Drug Radiation Research Department, National Center for Radiation Research and Technology (NCRRT), Egyptian Atomic Energy Authority (EAEA), Cairo, Egypt

³ Materials Science and Nanotechnology Department, Faculty of Postgraduate Studies for Advanced Sciences (PSAS), Beni-Suef University, Beni-Suef 62511, Egypt

1 Introduction

Semiconductors based-photocatalysts that have used light radiation energy to remove contaminants have become highly innovative and environmentally beneficial solutions. Removing organic pollutants in sewerage discharge can be a challenging issue. It is crucial to find an appropriate solution to pollutants and promote feasible and eco-friendly techniques [1]. A notable functional photocatalyst has to possess excellent absorption of assisted radiation. Besides, the photo-induced electron–hole pairs caused by exposure to light irradiation should have been isolated to allow the reduction and oxidation reactions adequate time. Even so, photocatalytic degradation is hampered by considerable challenges like the confined area of the absorption of illumination and the limited extraction efficiency of the employed photocatalysts, and this will not be able to address the needs of practical applications [2]. As a result, in current photocatalytic research, the investigation

of unique photocatalysts with remarkable efficiency and stability is a modernistic and innovative responsibility [3].

The molybdenum disulfide (MoS_2) has shown great promise in many applications [4, 5]. MoS_2 is a potential semiconductor photocatalyst as a transition metal dichalcogenide because of its excellent visible-light sensitivity, small bandgap, relatively inexpensive, and lack of toxicity [2, 6–8]. MoS_2 , like a graphene, is a 2D nanomaterial with exceptional breaking tensile strength [9]. Nevertheless, due to its weak intrinsic conductivity and speedy photoinduced electron–hole recombination, MoS_2 possesses restricted catalytic activity. Consequently, finding an appropriate modification strategy to boost MoS_2 's photocatalytic activity remains a challenge [10].

In this vein, spinel cobaltites MCo_2O_4 ($\text{M} = \text{Zn, Ni, Mn, ...}$) as magnetic photocatalysts have revealed outstanding photocatalytic activity by displaying the photo-induced electron/holes to eliminate the organic contaminants [11–13]. ZnCo_2O_4 has been widely used in photodegradation as a p-type semiconductor and binary metal oxide of the spinel cobaltite family. As a result of its wide-range UV–visible ray absorption (200–800 nm), ZnCo_2O_4 is suitable for organic photodegradation utilizations [14–16]. As a result, adding MoS_2 to the ZnCo_2O_4 photocatalyst will improve visible light absorption and reduction reactions in the conduction band while increasing the surface area available for the photocatalytic process. Besides, the ZnCo_2O_4 possesses magnetic nature and can act as a recyclable magnetic catalyst for ease of separation from the water after treatment [17].

In addition, previous research has displayed that the coating photocatalysts with a host of exciting layers, including such silver Ag and gold Au elements, enhanced the photocatalytic activity due to reducing the rate of the recombination process for induced-charge carriers [18]. Due to “it’s localized surface Plasmon resonance” (LSPR) absorption, silver NPs boost light absorption and work as sinks for photogenerated charge carriers, preventing charge carrier recombination in composites. At the metal/semiconductor interface, noble metals with Fermi levels lower than the semiconductor photocatalyst’s conduction band level initiate a Schottky junction. Photoinduced electrons may be successfully trapped by metals, enhancing the separation of electrons and holes as a result [19–21]. So, can enhanced the catalysts process by combining Ag nanoparticles to $\text{ZnCo}_2\text{O}_4/\text{MoS}_2$. So, Ag NPs were decorated on the surface of $\text{ZnCo}_2\text{O}_4/\text{MoS}_2$, that the electron–hole separation can be enhanced by the improved conductivity of the interface between ZnCo_2O_4 and MoS_2 . Yuefa et al. [22] have reported that Au NPs enhanced $\text{CoFe}_2\text{O}_4\text{–MoS}_2$ photocatalyst to degrade methyl orange by using visible light irradiation. Also, Junwei et al. [23] have improved photocatalytic hydrogen generation of $\text{TiO}_2\text{–Cu}_2\text{O}$ composite by adding Ag.

An essential biomedical application of NPs is their use as innovative antimicrobial agents, which overcomes the drawbacks of synthetic antimicrobial drugs [24–26]. NPs have diverse mechanisms of action to kill pathogenic microorganisms, such as oxidative stress and metal ion release [27]. It has been proven that the smaller the particle size, the better antimicrobial activity [28]. Ag NPs were known as antibacterial and antifungal materials, which depend on their shape and size and after congregation with different active composite to increase their activity at low concentration to avoid the toxicity as reported in recent studies [29–32]. Baraka et al. [33] synthesized green Ag NPs using natural pigments extracted from Alfalfa leaves. The synthesized Ag NPs possessed a superior antimicrobial activity towards *S. aureus* ATCC 29213; 24.0 mm ZOI, followed by *E. coli* ATCC 25922; 17.0 mm ZOI. In addition, Ag NPs were a strong antifungal agent against *C. albicans* ATCC 10231; 26.0 mm ZOI.

Recently, the utilization of γ -irradiation in the fabrication of metal NPs has been confirmed to have several favorable merits. The regulated reduction for metal ions can be achieved without utilizing an extra reducing factor or assembling any unwanted oxidation by-products. Besides, the rates of reactions begun by radiation are sufficiently defined. Furthermore, the reducing factor is uniformly created in the solution [34].

Herein, we have concentrated our efforts on gamma irradiation-assisted synthesis of Ag-decorated $\text{ZnCo}_2\text{O}_4/\text{MoS}_2$ heterostructure as a novel eco-friendly photocatalyst to degrade methylene blue MB and as effective antimicrobial agents. Ag NPs were decorated on the surface of $\text{ZnCo}_2\text{O}_4/\text{MoS}_2$; therefore, the segregation of electrons and holes can be improved by enriching the interface's conductivity between ZnCo_2O_4 and MoS_2 . As a result, it is essential to consider the unique characteristics of heterostructure Ag-decorated $\text{ZnCo}_2\text{O}_4\text{–MoS}_2$ photocatalysts for environment water purification.

2 Materials and Methods

2.1 Materials

Molybdenum disulfide (MoS_2) is purchased from PubChem CO., cobalt nitrate ($\text{Co}(\text{NO}_3)_2 \cdot 6\text{H}_2\text{O}$), zinc sulfate ($\text{ZnSO}_4 \cdot 7\text{H}_2\text{O}$), silver nitrate (AgNO_3), citric acid ($\text{C}_6\text{H}_8\text{O}_7 \cdot \text{H}_2\text{O}$), ethylene glycol ($\text{C}_2\text{H}_6\text{O}_2$) were acquired from Sigma Aldrich and employed as raw precursors.

2.2 Synthesis of Ag-Decorated $\text{ZnCo}_2\text{O}_4\text{–MoS}_2$

Firstly, the spinal ZnCo_2O_4 was synthesized via the sol–gel technique, as illustrated in Fig. 1 [35]. Secondly, 3 g of

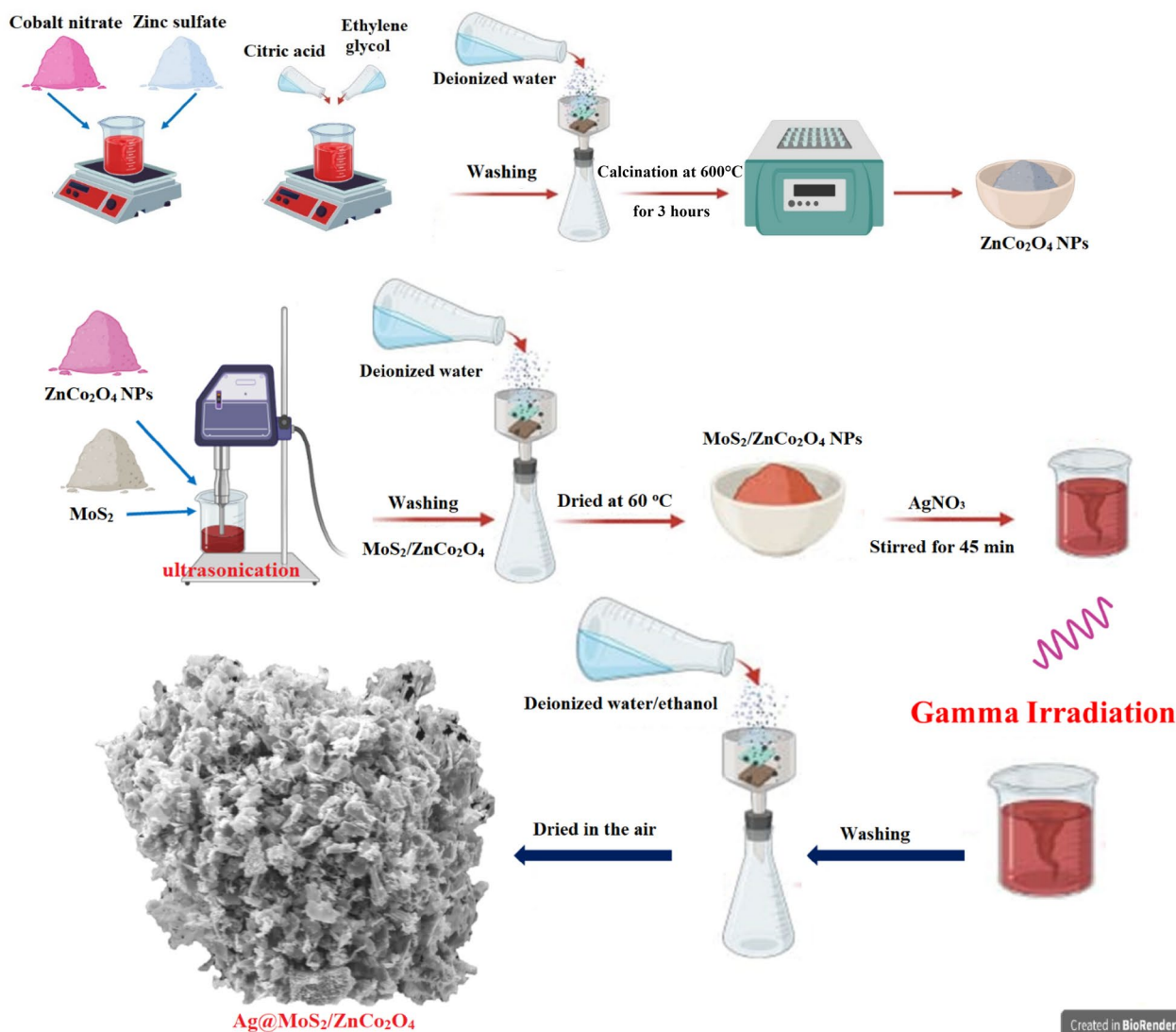


Fig. 1 Schematic diagram for synthesis of Ag decorated MoS₂-ZnCo₂O₄ NPs

the synthesized spinal ZnCo₂O₄ NPs and 1.5 g of molybdenum disulfide (MoS₂) were strongly distributed in the ethanol into the ethanol and deionized water (70/30 v/v). The mixture was homogenized utilizing ultrasonication for 45 min to even get a homogeneous distribution. The product MoS₂-ZnCo₂O₄ was filtered and washed with deionized water several times and dried at 60 °C for 3 h. After that, 3 g of MoS₂-ZnCo₂O₄ NPs and 0.5 g of silver nitrate (AgNO₃) were dissolved in 120 ml of deionized water and mixed under magnetic stirring for 45 min. Finally, the solution of the investigated samples was subjected to 50 kGy (dose rate of ~1.1 kGy/h) at ambient conditions. The irradiation was performed by utilizing Co-60 gamma-cell sources. The Ag-decorated ZnCo₂O₄-MoS₂ NPs were filtered and washed via a mixture of ethanol, and water was dried in the air to give Ag-decorated ZnCo₂O₄-MoS₂ NPs. The prepared samples

are characterized via X-ray diffractometer, Shimadzu XRD-6000, and scanning electron microscope (SEM), JEOL JSM-5600 LV, Japan). Also, UV diffusion reflectance spectra were measured via Jasco UV-Visible Spectrophotometer (V-670 PC).

2.3 Photocatalytic Activity Measurement

All photocatalytic tests were performed at ambient temperature (25 °C ± 2 °C). The Ag-decorated ZnCo₂O₄-MoS₂ nanocomposite was dipped in a methylene blue aqueous environment under vigorous stirring. The MB dye solution and the spinal ZnCo₂O₄, MoS₂, and Ag-decorated ZnCo₂O₄-MoS₂ nanocomposite photocatalysts were stirred in the dark for 30 min to specify adsorption-desorption equilibrium. Then, the dye solution having the MoS₂, the spinal

ZnCo₂O₄, and Ag-decorated ZnCo₂O₄–MoS₂ nanocomposite photocatalysts were illuminated by employing a metal halide lamp of 400 W. MB's final concentration (C₁) and the percentage removal of MB were evaluated by utilizing Ref. [36].

2.4 Antimicrobial Activity

The synthesized MoS₂, the spinal ZnCo₂O₄, and Ag-decorated ZnCo₂O₄–MoS₂ nanocomposite samples were tested for their antimicrobial potential upon selected pathogens (yeast and bacteria) throughout the agar-disc diffusion method [31, 37].

The activity of the as-synthesized samples had examined against different types of Gram-positive, and Gram-negative bacteria, such as *Staphylococcus aureus*, *Pseudomonas aeruginosa*, *Proteus mirabilis*, *Escherichia coli*, *Klebsiella pneumoniae*, *Salmonella typhi*, *Bacillus subtilis*, and *Proteus vulgaris*. The zone of inhibition (ZOI) was displayed after 24 hrs. of incubation and is a suitable parameter regarding the hindrance of microbial growth [38]. *Candida albicans* and *Candida tropicalis* were an example of pathogenic unicellular fungi used to evaluate the antifungal potency of the synthesized samples. Before the ZOI testing, the microbial inoculums must be standardized according to 0.5 McFarland (at 600 nm) and fixed from 2–5 × 10⁸ CFU/mL for bacteria and 1–4 × 10⁸ CFU/mL for the tested yeast. Positive standard antibiotics Nystatin (NS) and Amoxicillin (AX) were used to evaluate the ZOI potency [31].

2.5 Potential Antibiofilm Behavior

The synthesized MoS₂ NPs, the spinal ZnCo₂O₄ NPs, and Ag-decorated ZnCo₂O₄–MoS₂ nanocomposite were tested for their potency as antibiofilm agents after conducting biofilm tube method. The anti-biofilm of the synthesized nanocomposites was investigated upon the chosen bacteria and *Candida* spp. and was persistent and corresponded with the control (non-treated one). A qualitative test about biofilm repression was noted by Christensen et al. [39].

The microbial inoculums had been adjusted according to 0.5 McFarland and fixed from 1–3 × 10⁸ CFU/mL, and were incubated for 1 day at 37.0 ± 0.5 °C. A 5.0 mL nutrient broth medium was mixed with the tested samples inside distinct test tubes. After the incubation time, all the media components in the treated and control (cell-free supernatant) were discarded. All tubes were washed with phosphate buffer saline (PBS; pH 7.0), and after that, all tubes were cleaned with deionized water [40]. The resulted cells inside tube walls were fixed with 5.0 mL (3.5%) sodium acetate for 20 min, and finally, they were washed with de-ionized water. If the result is positive, the created biofilm was stained with (0.15%) crystal violet (CV) and,

after the staining process, washed with de-ionized water to remove the excess CV. At the end of the experiment, about 5.0 mL of absolute ethanol was added to measure the semi-quantitative analysis of the anti-biofilm potential. UV–Vis. examined the stained microbial biofilms with a CV applying UV–Vis. spectrophotometer at 570.0 nm. The microbial biofilms repression percentage was calculated by using the following Eq. (1) [39].

$$\begin{aligned} & \text{Percentage of bacterial and yeast biofilm inhibition(\%)} \\ & = \frac{\text{O.D. of the control sample} - \text{O.D. of the treated sample}}{\text{O.D. of the control sample}} \times 100 \quad (1) \end{aligned}$$

2.6 Growth Curve Assay

The influence of MoS₂, the spinal ZnCo₂O₄, and Ag-decorated ZnCo₂O₄–MoS₂ nanocomposite on the growth of *S. aureus* (the most sensitive microbes) was determined by the growth curve assay according to Huang et al. [41]. The microbial suspension was adapted to 0.5 McFarland (1 × 10⁸ CFU/mL) in 5.0 ml of nutrient broth tubes. MoS₂, the spinal ZnCo₂O₄, and Ag-decorated ZnCo₂O₄–MoS₂ nanocomposite were included separately in the examined tubes. The absorbance of the microbial growth following treatment was evaluated each 2 hrs. intervals up to 24 hrs. (Wavelength of 600 nm). The relationship had been conducted between the average of duplicate readings and a time to obtain the typical growth curve.

2.7 Potential Effect of UV Illumination

Two hours incubated, bacterial cultures were established to standard 0.5 McFarland (1 × 10⁸ CFU/mL). MoS₂, the spinal ZnCo₂O₄, and Ag-decorated ZnCo₂O₄–MoS₂ nanocomposite were incorporated into the estimated tubes. After illumination with UV, the antimicrobial potency of the synthesized MoS₂, the spinal ZnCo₂O₄, and Ag-decorated ZnCo₂O₄–MoS₂ nanocomposite was tested towards *S. aureus* operating the optical density method in comparison with the control non-UV irradiation [31].

The tubes were categorized as two states, tubes containing non-UV irradiated MoS₂, the spinal ZnCo₂O₄, and Ag-decorated ZnCo₂O₄–MoS₂ nanocomposite and tubes with MoS₂, the spinal ZnCo₂O₄, and Ag-decorated ZnCo₂O₄–MoS₂ nanocomposite and UV-irradiated which was exhibited to different periods as 0, 15, 30, 45, 60, and 75 min and the intensity was determined as 6.9 mW cm⁻² disturbance on the samples at 37 °C, and the sample turbidity was assessed at 600 nm. The inhibition % was defined by Eq. (1), according to Abd Elkodous et al. [42].

2.8 Effect of the Synthesized Nanocomposites on Bacterial Protein Leakage

Fresh 18 hrs. bacterial culture (*S. aureus*) was fixed at 1×10^8 CFU/mL, and the synthesized MoS_2 , the spinal ZnCo_2O_4 , and Ag-decorated ZnCo_2O_4 – MoS_2 nanocomposite were combined with 10 mL of the nutrient broth. MoS_2 -, the spinal ZnCo_2O_4 -, and Ag-decorated ZnCo_2O_4 – MoS_2 nanocomposite-free broth mixed with culture were utilized as the control. The treated samples were incubated for 5 hrs. (37°C) and then centrifuged at 5500 rpm for 15 min [43]. The resulted supernatant (100 μL) for the examined samples was combined with Bradford reagent (1 mL). Optical density was assessed after 10 min of dark incubation (at 595 nm) [43].

2.9 Reaction Mechanism Determination by SEM

The tested *S. aureus* was washed with PBS and fixed with 3.5% glutaraldehyde. After that, the fixed *S. aureus* was washed repeatedly with PBS and rinsed with ethanol at 27°C for 20 min before dehydration. Finally, *S. aureus* was fixed and set over the aluminum stump to start the SEM imaging. The treated and untreated *S. aureus* morphological and surface features with the examined Ag-decorated ZnCo_2O_4 – MoS_2 nanocomposite was tested using SEM imaging.

2.10 Statistical Determination

The ONE WAY ANOVA (at $P < 0.05$) was conducted to determine the statistical investigation of the obtained results and arranged as a Duncan's multiple sequence analyses [44]. The results were examined and studied via SPSS software version 15.

3 Results and Discussions

3.1 Characterization of the Investigated Photocatalysts

The XRD patterns of MoS_2 , the spinal ZnCo_2O_4 , and Ag-decorated ZnCo_2O_4 – MoS_2 nanocomposite samples are shown in Fig. 2. Figure 2 exhibited the XRD pattern of ZnCo_2O_4 NPs. The detected peaks at $2\theta = 19.19^\circ$ (111), 31.44° (220), 36.97° (311), 44.86° (400), 55.76° (422), 59.58° (511), and 65.42° (440) are in good matching with the standard cards of JCPDS No. 23-1390. These peaks have belonged to the Fd3m space group of those of spinel ZnCo_2O_4 NPs [45]. Further, the peaks that have been seen of bulk MoS_2 were unique for 2H- MoS_2 with a distinctive peak detected at $2\theta = 14.42^\circ$ (002) which are in

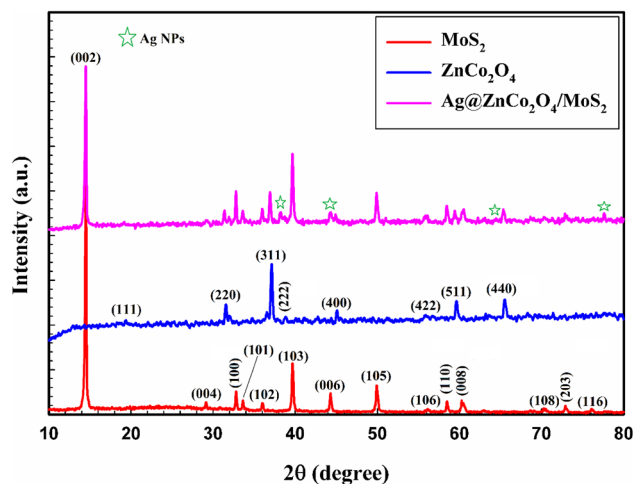


Fig. 2 XRD patterns of MoS_2 , the spinal ZnCo_2O_4 , and Ag decorated MoS_2 – ZnCo_2O_4 nanocomposite samples

good matching with the phase of the hexagonal MoS_2 (JCPDS: 37-1492). Also, the appearance of the distinctive peak with the plane (002) proved that the exfoliated MoS_2 nanosheets have existed [46–50]. At the same time, the Ag-decorated ZnCo_2O_4 – MoS_2 nanocomposite sample showed characteristic peaks of Ag NPs at $2\theta = 38.15^\circ$ (111), 44.27° (200), 64.68° (220), and 77.66° (311) (JCPDS 4-0783) [51, 52]. Also, the crystallite size of Ag-decorated ZnCo_2O_4 – MoS_2 nanocomposite is found of 47.25 nm via using the Debye–Scherer formula [53]. The XRD results for MoS_2 , the spinal ZnCo_2O_4 , and Ag-decorated ZnCo_2O_4 – MoS_2 nanocomposite samples confirmed the successful preparation and purity of the studied samples [31].

Figure 3 showed the surface morphology of MoS_2 , the spinal ZnCo_2O_4 , and Ag-decorated ZnCo_2O_4 – MoS_2 nanocomposite samples. Figure 3A revealed that the Ag-decorated ZnCo_2O_4 – MoS_2 nanocomposite sample possesses a heterogeneous structure. Where SEM image of MoS_2 exhibited a disordered array of nanoflakes shape for exfoliated MoS_2 sample (Fig. 3B) [54]. Also, Fig. 3C revealed the spherical shape nature of the spinal ZnCo_2O_4 NPs. Similar observed surface morphology is seen in previous work [29].

EDX spectra and elemental mapping images were addressed to present the elemental composition and distribution of the sample. Figure S1 shows the EDX spectra of the Ag-decorated ZnCo_2O_4 – MoS_2 nanocomposite. Every one of the elements in the Ag-decorated ZnCo_2O_4 – MoS_2 nanocomposite can be viewed (such as Ag, Zn, Co, O, C, Mo, and S) with stoichiometric ratios. At the same time, the appearance of the carbon (C) peak is attributable to the citric acid used in the preparation of the spinal ZnCo_2O_4 NPs. Furthermore, the elemental mapping images Ag-decorated ZnCo_2O_4 – MoS_2 nanocomposite proved all fundamental elements are homogeneously distributed (Fig. 4). Also,

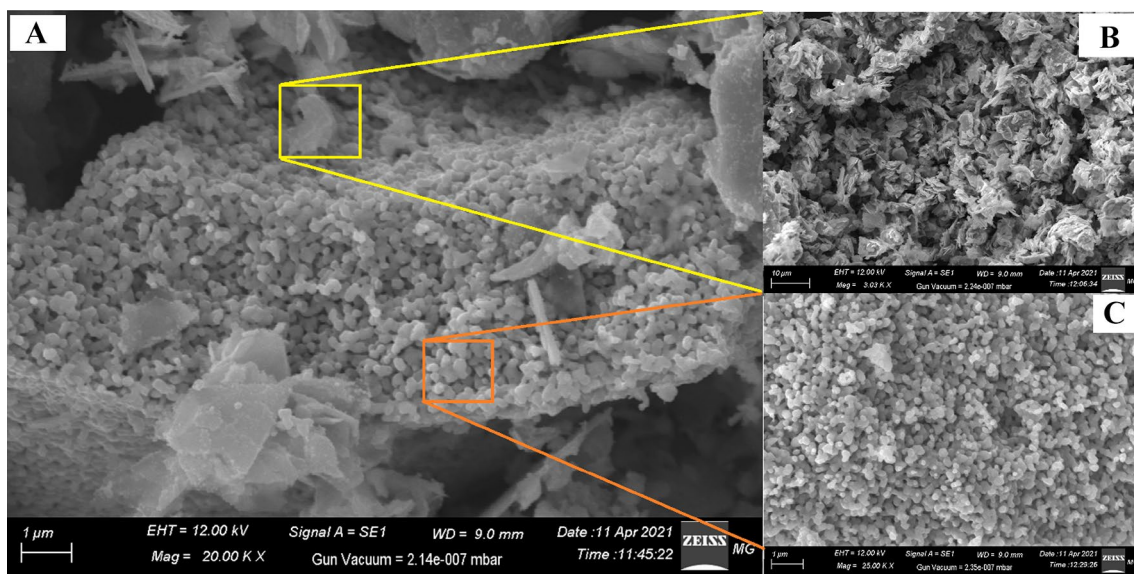


Fig. 3 SEM images of **A** Ag decorated MoS₂-ZnCo₂O₄ nanocomposite, **B** MoS₂, and **C** the spinal ZnCo₂O₄ NPs

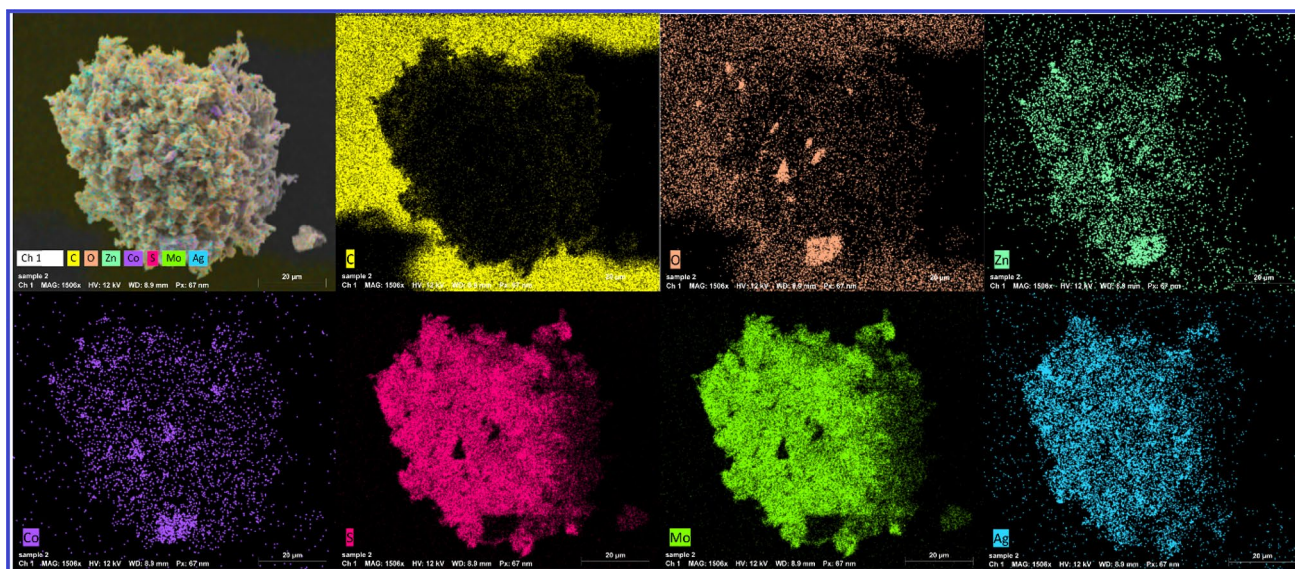


Fig. 4 The elemental mapping images Ag decorated MoS₂-ZnCo₂O₄ nanocomposite

HR-TEM images confirmed the conjugation of Ag NPs with MoS₂-ZnCo₂O₄ NPs (composite external layer), as shown in Fig. 5. Further, the TEM images confirmed that the particles of Ag-decorated ZnCo₂O₄-MoS₂ nanocomposite possessed nearly spherical shapes, with an average diameter in nanoscale.

Figure S2 shows the typical diffuse reflectance spectra (DRS) of MoS₂, the spinal ZnCo₂O₄, and Ag-decorated ZnCo₂O₄-MoS₂ nanocomposite samples. The wavelength at maximum reflection (λ_{\max}) for MoS₂, the spinal ZnCo₂O₄, and Ag-decorated ZnCo₂O₄-MoS₂ nanocomposite samples

was found to be within 200 and 300 nm, as can be seen in the figure. Besides, the optical band gap for MoS₂, the spinal ZnCo₂O₄, and Ag-decorated ZnCo₂O₄-MoS₂ nanocomposite samples can be evaluated via the reflectance results via Kubelka-Munk theory and Tauc's equation [55, 56]. The observed optical bandgap (E_g) for MoS₂, the spinal ZnCo₂O₄, and Ag-decorated ZnCo₂O₄-MoS₂ nanocomposite samples is 2.31, 2.68, and 2.52 eV, respectively, as illustrated in Fig. S3. When compared to ZnCo₂O₄ and MoS₂ NPs, the absorption band edge of Ag-decorated ZnCo₂O₄-MoS₂ nanocomposite deposited with Ag was

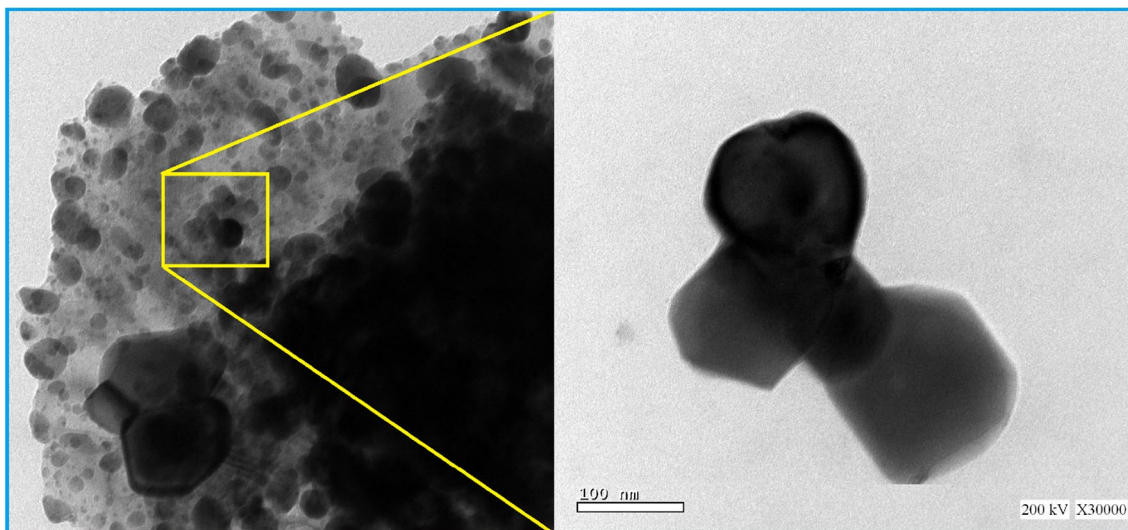


Fig. 5 TEM images of Ag decorated MoS_2 - ZnCo_2O_4 nanocomposite

red-shifted i.e. decrease of optical bandgap. This may be interpreted by the LSPR effect of loaded Ag NPs, which enhanced the photocatalytic performance by broadening visible light's absorption range and speeding up the separation rate of photoexcitation charging [19–21].

4 Photocatalytic Activity of the Investigated Samples

4.1 Effect of Initial pH Value

Due to various reaction mechanisms that can affect dye degradation, determining the effect of pH on photodegradation rate is a complicated process [57]. Contribution depends on the photocatalyst's characteristics and pH value [58–60]. The influence of solution pH on the rate of MB removal in the presence of MoS_2 , the spinal ZnCo_2O_4 , and Ag-decorated ZnCo_2O_4 - MoS_2 nanocomposite photocatalysts is illustrated via using 10 mg of the photocatalysts for 1×10^{-5} M of MB (Fig. 6a–j). The absorbance spectrum of MB, which displayed a noticeable absorption wavelength around 665 nm ($\lambda_{\text{max}} = 600\text{--}700$ nm), was well-matched with early-declared investigations [61–63]. In alkaline solution (pH 12), the investigated photocatalysts showed an exceptional reduction of the MB concentration compared to the neutral and acidic conditions as well as MB dye removal due to adsorption in the dark. It was evident that the adsorption in the dark declined about 43%, 23.6%, and 6.3% of the dye at 30 min by using the MoS_2 , the spinal ZnCo_2O_4 , and Ag-decorated ZnCo_2O_4 - MoS_2 nanocomposite photocatalysts, respectively. It is observed that both MoS_2 and ZnCo_2O_4 exhibited 89%, 90.5% degradation efficiency of the MB at

pH 12, respectively, as illustrated in Fig. 6a and c. In the same context, the Ag-decorated ZnCo_2O_4 - MoS_2 nanocomposite exhibited high efficiency of MB dye decolorization; about 95.4% removal of the dye at pH 12 was achieved after 180 min under light, as presented in Fig. 6b. In comparison, MB degradation simultaneously reached about 66% and 69% from its original concentration using Ag-decorated ZnCo_2O_4 - MoS_2 nanocomposite photocatalyst in the neutral (i.e., pH 7) and acidic (i.e., pH 4) environments, respectively. The degradation of MB is significantly rapid in alkaline environments than in neutral or acidic ones. The electrostatic interaction between the MB molecules and the Ag-decorated ZnCo_2O_4 - MoS_2 nanocomposite photocatalyst is responsible for this outcome leading to the enhancement of redox reactions [64]. This indicates the significance of Ag NPs in boosting charge transfer between the ZnCo_2O_4 - MoS_2 interface.

4.2 Effect of Photocatalysts Dose and Initial MB Concentration

As shown in Fig. 7, the effect of the photocatalysts dose on photocatalytic performance was investigated. The effect of the photocatalysts dose on MB degradation under light illumination was examined by changing the amount of the utilized photocatalysts (5 and 20 mg) at pH 12. Whenever the dosage of nanocomposite photocatalyst in aqueous MB solution was varied from 5 to 20 mg, the percentage of MB removal increased from 83.6 to 94.5% after 150 min of irradiation for light. It is ascribing that the enhancement of the amount of photocatalyst leads to the enrichment of the number of active sites obtainable for MB reduction [65]. In other terms, having a lot of active sites on the surface of

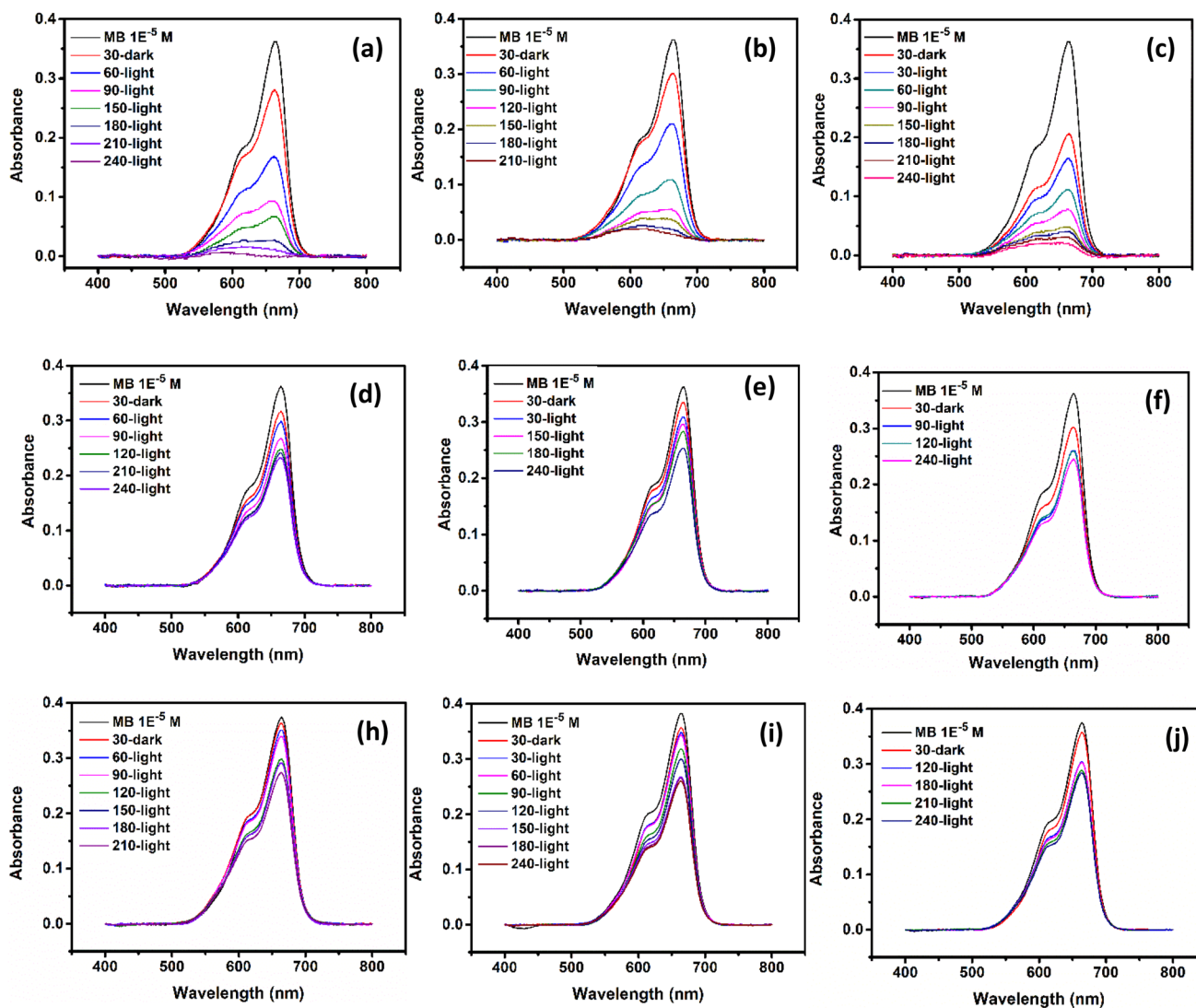


Fig. 6 Degradation of MB 1×10^{-5} M, and 10 mg from **a** ZnCo_2O_4 , **b** composite and **c** MoS_2 at pH 12, **d** ZnCo_2O_4 , **e** composite and **f** MoS_2 at pH 8 and **h** ZnCo_2O_4 , **i** composite and **j** MoS_2 at pH 4

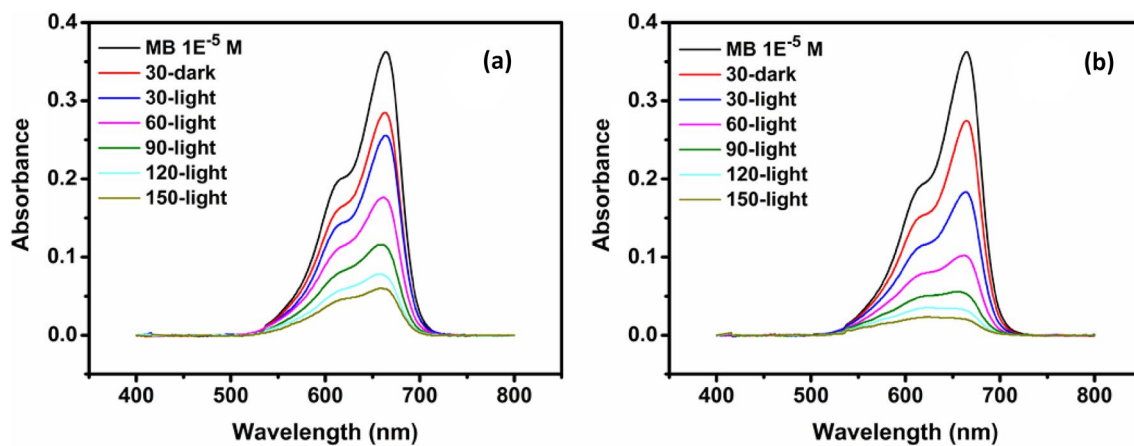


Fig. 7 Degradation of MB 1×10^{-5} M at pH 12 using **a** 5 mg and **b** 20 mg from Ag decorated MoS_2 - ZnCo_2O_4 nanocomposite

the photocatalyst used will increase the number of absorbed photons, resulting in more electrochemical reactions and improved performance [65]. As a result, numerous charge carriers and free radicals will most obviously be produced.

Furthermore, a specified amount of adsorbent can only absorb a certain amount of adsorbate molecules. As a result, the appropriate amount of the initial concentration of the adsorbate solution must be evaluated. Variable initial MB concentrations (5×10^{-6} and 5×10^{-5} M) are being used to explore the effects of MB initial concentration on the photodegradation efficiency of Ag-decorated $\text{ZnCo}_2\text{O}_4\text{-MoS}_2$ nanocomposite photocatalyst (Fig. 8). The amount of MB eliminated over time dropped as the MB initial concentration was increased. The percentage amount of MB elimination dropped from 93.07% to 51.07% at 120 min as the initial MB concentration was increased from 5×10^{-6} to 5×10^{-5} M [66–68].

4.3 Reaction Kinetics and Apparent Rate Constant

This can be seen in Fig. 9, the reaction kinetics of MB degradation under light irradiation through synthesized Ag-decorated $\text{ZnCo}_2\text{O}_4\text{-MoS}_2$ nanocomposite photocatalyst followed very well the pseudo-first-order model. In addition, it was observed that the value of reaction rate constant k decreased with increasing the initial concentration of MB. In contrast, it increases with enriching the nanocomposite photocatalyst dose, consistent with the degradation performance [69].

Based on the given findings, we provide a suggestion to the MB photodegradation mechanism via the Ag-decorated $\text{ZnCo}_2\text{O}_4\text{-MoS}_2$ nanocomposite photocatalyst using Fig. 10. Generally, the free radicals (h^+ , $\text{O}_2^{\cdot-}$, OH^{\cdot}) possess predominant roles in the photodegradation of organic dye residuals. Likewise, Z-scheme-based on Au decorated $\text{CoFe}_2\text{O}_4/\text{MoS}_2$ photocatalyst was previously reported [22]; it will be more proper to

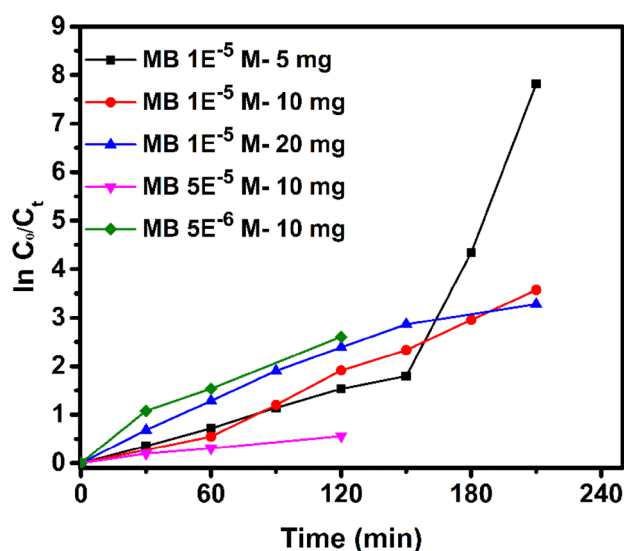


Fig. 9 Pseudo first-order kinetics plots for MB degradation by using Ag decorated $\text{MoS}_2\text{-ZnCo}_2\text{O}_4$ photocatalyst

assume that the presence of Ag NPs at the surface of ZnCo_2O_4 and MoS_2 can enrich the interface conductivity. This leads to the recombination inducing for the electrons from the conduction band (CB) of ZnCo_2O_4 with the holes in the valence band (VB) of MoS_2 . Consequently, incorporating Ag NPs can provide the most acceptable pathway for electron transfer, which is the principal explanation for the excellent photocatalytic potential for Ag-decorated $\text{ZnCo}_2\text{O}_4\text{-MoS}_2$ nanocomposite photocatalyst.

Thus, the photodegradation of MB utilizing Ag-decorated $\text{ZnCo}_2\text{O}_4\text{-MoS}_2$ nanocomposite photocatalyst may be described as follows:

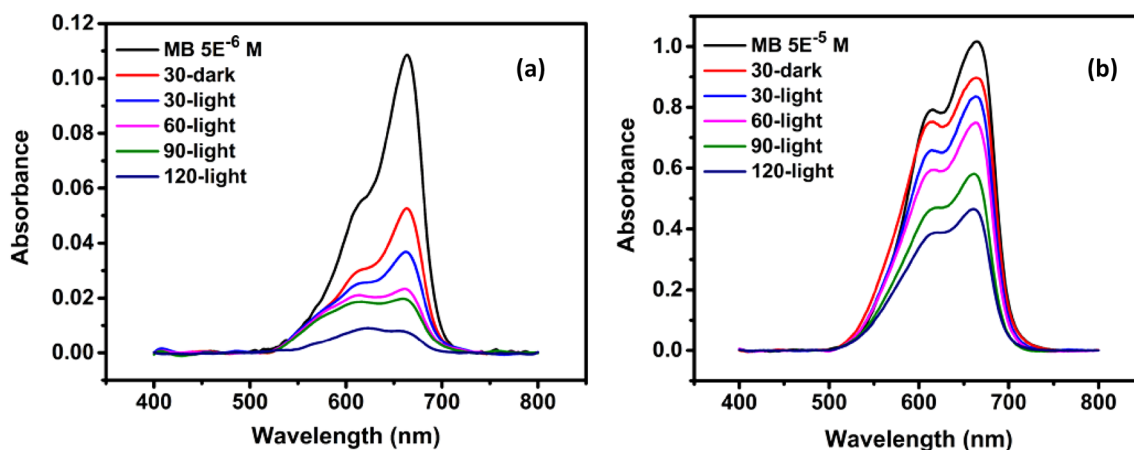
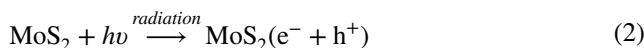


Fig. 8 Degradation of MB using 10 mg of Ag decorated $\text{MoS}_2\text{-ZnCo}_2\text{O}_4$ nanocomposite at pH 12 for a 5×10^{-6} M and b 5×10^{-5} M of MB

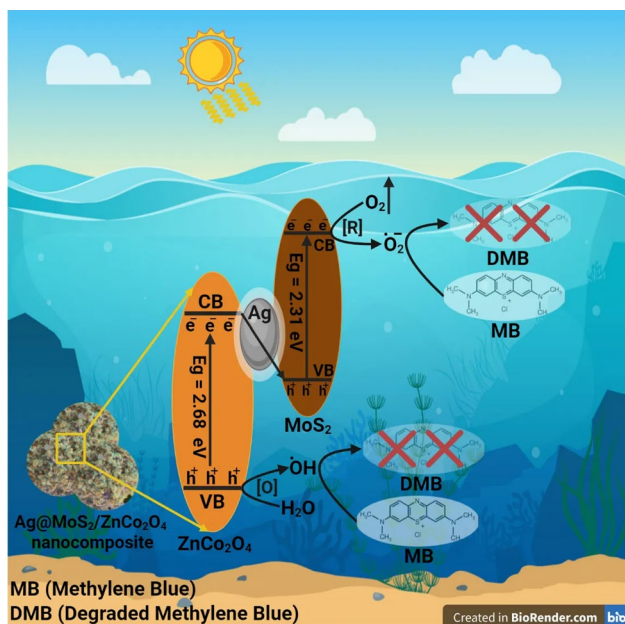
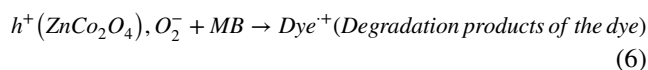
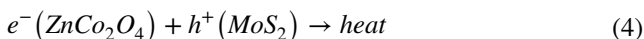
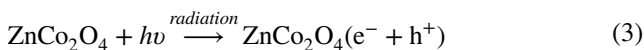


Fig. 10 Reaction mechanism for MB degradation by using Ag decorated $\text{MoS}_2\text{-ZnCo}_2\text{O}_4$ photocatalyst



4.4 Antimicrobial Activity

It was determined that some antibiocal agents were operated to prevent microbial diseases, and with time the microbe received a resistance [31]. New methods and materials were used to create unexplored antimicrobial agents, particularly those used to manage spreading diseases [70].

The antimicrobial action of all the synthesized MoS_2 , the spinal ZnCo_2O_4 , and Ag-decorated $\text{ZnCo}_2\text{O}_4\text{-MoS}_2$ nanocomposite is concerned at a selected concentration ($10 \mu\text{g/mL}$) by a disc agar diffusion assay [30]. The tested samples display a positive potency to a wide spectrum of bacteria like *P. mirabilis*, *S. aureus*, *P. aeruginosa*, and *C. albicans*. In particular, Ag-decorated $\text{ZnCo}_2\text{O}_4\text{-MoS}_2$ nanocomposite possessed the highest impact, followed by the spinal ZnCo_2O_4 NPs towards all the tested pathogenic microbes, as mentioned in Table 1 and Fig. 11.

The synthesized samples was effective against Gram-positive bacteria more than Gram-negative ones. The Gram-negative cell wall consisted mainly of lipopolysaccharide (protective layer) and thin peptidoglycan. The antimicrobial potency of the synthesized samples had been compared with the standard antibiotics (AX & NS), which are more influential than all. At the same time, Gram-positive possesses

Table 1 Antibacterial and antifungal potential of MoS_2 NPs, the spinal ZnCo_2O_4 NPs, and Ag-decorated $\text{ZnCo}_2\text{O}_4\text{-MoS}_2$ nanocomposite as ZOI (mm), and MIC ($\mu\text{g/mL}$)

Pathogenic microbes	MoS_2 NPs		ZnCo_2O_4 NPs		Ag-decorated $\text{ZnCo}_2\text{O}_4\text{-MoS}_2$ nanocomposite		^a AX and NS
	ZOI (mm)	MIC ($\mu\text{g/mL}$)	ZOI (mm)	MIC ($\mu\text{g/mL}$)	ZOI (mm)	MIC ($\mu\text{g/mL}$)	
<i>Staphylococcus aureus</i>	$8.5 \pm 0.1259^{\text{ef}}$	2.5	$13.2 \pm 0.7600^{\text{g}}$	0.312	$25.6 \pm 0.2259^{\text{h}}$	0.019	$6.5 \pm 0.2155^{\text{a}}$
<i>Pseudomonas aeruginosa</i>	$7.1 \pm 0.5424^{\text{c}}$	5.0	$10.3 \pm 0.5800^{\text{e}}$	0.625	$21.3 \pm 0.1596^{\text{g}}$	0.039	$12.0 \pm 0.3650^{\text{f}}$
<i>Escherichia coli</i>	$6.2 \pm 0.7600^{\text{a}}$	10.0	$8.2 \pm 0.5300^{\text{b}}$	1.25	$16.2 \pm 0.1599^{\text{d}}$	0.156	$8.9 \pm 0.2155^{\text{bc}}$
<i>Klebsiella pneumoniae</i>	$6.3 \pm 0.2356^{\text{ab}}$	5.0	$7.1 \pm 0.5300^{\text{a}}$	1.25	$12.8 \pm 0.1599^{\text{a}}$	0.315	Nil
<i>Bacillus subtilis</i>	$8.3 \pm 0.3669^{\text{e}}$	2.5	$8.9 \pm 0.6900^{\text{b}}$	1.25	$13.5 \pm 0.1599^{\text{b}}$	0.315	$7.2 \pm 0.2155^{\text{b}}$
<i>Proteus vulgaris</i>	$8.1 \pm 0.2356^{\text{c}}$	5.0	$9.8 \pm 0.2359^{\text{cd}}$	0.625	$14.9 \pm 0.6800^{\text{e}}$	0.156	$8.5 \pm 0.1111^{\text{cd}}$
<i>Salmonella typhi</i>	$7.5 \pm 0.1259^{\text{cd}}$	5.0	$9.5 \pm 0.1259^{\text{c}}$	0.625	$13.2 \pm 0.1596^{\text{b}}$	0.315	$8.0 \pm 0.5000^{\text{ec}}$
<i>Proteus mirabilis</i>	$8.4 \pm 0.2356^{\text{b}}$	2.5	$10.0 \pm 0.5000^{\text{e}}$	0.625	$19.2 \pm 0.1599^{\text{e}}$	0.078	$10.0 \pm 0.2356^{\text{f}}$
<i>Candida albicans</i>	$9.2 \pm 0.5000^{\text{g}}$	2.5	$14.0 \pm 0.2356^{\text{g}}$	0.156	$22.2 \pm 0.1599^{\text{g}}$	0.039	$6.5 \pm 0.5000^{\text{a}}$
<i>Candida tropicalis</i>	$8.1 \pm 0.6850^{\text{e}}$	5.0	$12.5 \pm 0.1596^{\text{f}}$	0.625	$20.1 \pm 0.1599^{\text{f}}$	0.078	$9.5 \pm 0.6800^{\text{e}}$

Nil means that no ZOI had been measured.

^aAX Amoxicillin (antibacterial standard), NS Nystatin (antifungal standard), ZOI Zone of Inhibition, MIC Minimum Inhibitory Concentration.

Values are means \pm SD (n = 3).

Data within the groups are analyzed using one-way analysis of variance (ANOVA) followed by ^{a, b, c, d, e, f, g, h}Duncan's multiple range test (DMRT).

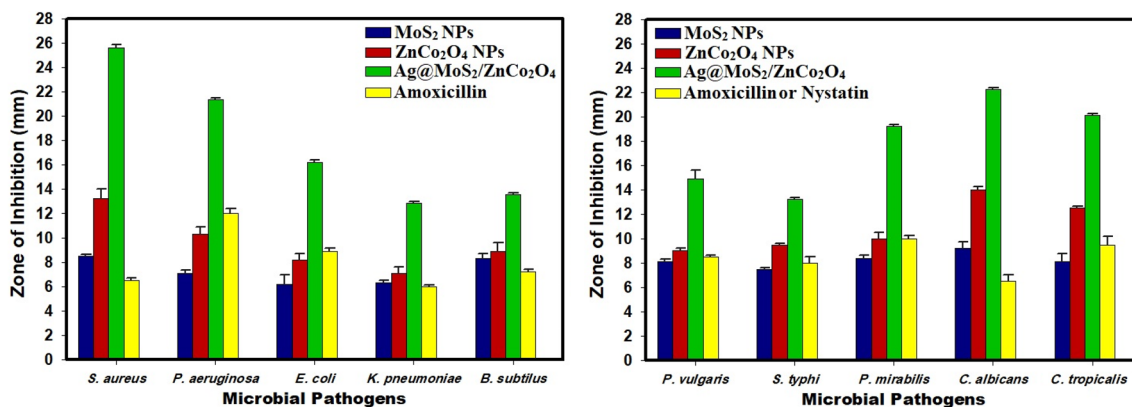


Fig. 11 Antibacterial and antifungal potential of MoS₂ NPs, the spinal ZnCo₂O₄ NPs, and Ag decorated MoS₂–ZnCo₂O₄ nanocomposite as ZOI (mm)

a thick peptidoglycan building coating [30]. It should be mentioned that basic formatting (the purity), sample configuration, and conjugated metal NPs should be evaluated to comprehend the antimicrobial characteristics [31].

It should be stated that there is applicability between the features of the prepared sample and the results monitored. They maintained appropriate physical and chemical effects over synthetic organic and manufactured antimicrobial agents, such as more formal interaction relationships, allowing for more helpful relations with more microbial cells, thus, improving their antimicrobial activity [71]. The dimensions and chemical configuration of the prepared samples was not the most significant parameter controlling their antimicrobial effects; different factors as purity, conjugation with active metal NPs, and strength should be evaluated [72].

The antimicrobial reaction means of samples is still not detected. The prepared models alter the bacterial morphology and its coating network, change the microbial membrane permeability and construct the existence of oxidative pressure response genes inside the microbial cell due to the creation of H₂O₂. Reactive oxygen species (ROS) diffusion was a superoxide anion (O₂⁻) and were suggested as an effective mechanism [73], the connection between the prepared samples with the microbial cell, following depleting the pathogenic microbes. Another antimicrobial activity mechanism had been investigated, like an alkaline attraction [30].

4.5 Antibiofilm Activity

Biofilm formation was specified in different exo-polysaccharide-producing pathogenic microbes [40]. Biofilm produced by the pathogenic bacteria in the lack and presence of MoS₂ NPs, the spinal ZnCo₂O₄ NPs, and Ag-decorated ZnCo₂O₄–MoS₂ nanocomposite was assessed operating the tube method [31].

Results described the stage of tube method for the anti-biofilm potential of MoS₂, the spinal ZnCo₂O₄, and Ag-decorated ZnCo₂O₄–MoS₂ nanocomposite upon *S. aureus*, which inoculated without MoS₂, the spinal ZnCo₂O₄, and Ag-decorated ZnCo₂O₄–MoS₂ nanocomposite, created the air–liquid interface compact whitish-yellow matt, and adhered to the tube walls and appeared the blue color of the adhered microbial cells after CV staining. A deep blue solution was formed after softening CV by absolute ethanol. In addition, no blue color was constructed following ethanol treatment, and the adhesive bacterial cells color was faint (Figures not shown). Otherwise, the treated tubes inoculated by *S. aureus* in the presence of MoS₂, the spinal ZnCo₂O₄, and Ag-decorated ZnCo₂O₄–MoS₂ nanocomposite detected a negative result bacterial ring growth was restricted.

A spectrophotometer (set at 570.0 nm) is functioned. UV–Vis. spectrophotometer represents the inhibition % of biofilm produced by the pathogens. Stained CV-biofilm had been dissolved by ethanol, and the optical density was assessed to calculate the creation of microbial biofilm. The inhibition % had been tabulated in Table 2 and calculated the biofilm hindrance created by the synthesized samples. The highest inhibition of MoS₂, the spinal ZnCo₂O₄, and Ag-decorated ZnCo₂O₄–MoS₂ nanocomposite percentage was noted for *S. aureus* (61.85%, 73.94%, and 97.06%), followed by *C. albicans* (76.67%, 84.15% and 94.08%), and *P. aeruginosa* (59.84%, 66.79%, and 92.40%), respectively as illustrated in Table 2, and Fig. 12.

The synthesized MoS₂, the spinal ZnCo₂O₄, and Ag-decorated ZnCo₂O₄–MoS₂ nanocomposite hinder biofilm construction at its irreversible bonding step (also understood as the initial step) [74]. Nevertheless, the mechanical movement of the synthesized samples against biofilm construction has yet to be confirmed. The interpretation in the inhibitory percentage might be defined by many aspects, including antimicrobial action, bio-sorption, physical possessions,

Table 2 Semi-quantitative inhibition % of the biofilm production for non-treated and treated bacterial and yeast pathogens with MoS₂, the spinal ZnCo₂O₄, and Ag-decorated ZnCo₂O₄–MoS₂ nanocomposite

Pathogenic microbes	O.D. of crystal violet stain at 570.0 nm				Inhibition %		
	Control	MoS ₂ NPs	ZnCo ₂ O ₄ NPs	Ag-decorated ZnCo ₂ O ₄ –MoS ₂ nanocomposite	MoS ₂ NPs	ZnCo ₂ O ₄ NPs	Ag-decorated ZnCo ₂ O ₄ –MoS ₂ nanocomposite
<i>Staphylococcus aureus</i>	0.852 ± 0.0125 ^b	0.325 ± 0.0259 ^b	0.222 ± 0.0325 ^d	0.025 ± 0.0381 ^d	61.85	73.94	97.06
<i>Pseudomonas aeruginosa</i>	0.777 ± 0.0521 ^{cd}	0.312 ± 0.0555 ^d	0.258 ± 0.0259 ^c	0.059 ± 0.0325 ^c	59.84	66.79	92.40
<i>Escherichia coli</i>	0.569 ± 0.0259 ^a	0.201 ± 0.0159 ^a	0.189 ± 0.0145 ^a	0.149 ± 0.0125 ^a	64.64	66.78	73.81
<i>Klebsiella pneumoniae</i>	0.854 ± 0.0159 ^e	0.625 ± 0.0259 ^b	0.595 ± 0.0659 ^f	0.405 ± 0.0555 ^e	26.81	30.32	52.57
<i>Bacillus subtilis</i>	0.789 ± 0.0259 ^d	0.595 ± 0.0325 ^c	0.356 ± 0.0325 ^c	0.333 ± 0.0259 ^c	24.58	54.87	57.79
<i>Proteus vulgaris</i>	0.963 ± 0.0145 ^g	0.456 ± 0.0125 ^a	0.325 ± 0.0135 ^a	0.300 ± 0.0159 ^{ab}	52.64	66.25	68.84
<i>Salmonella typhi</i>	0.888 ± 0.0659 ^f	0.656 ± 0.0659 ^e	0.609 ± 0.0259 ^e	0.312 ± 0.0555 ^c	26.12	31.41	64.86
<i>Proteus mirabilis</i>	0.725 ± 0.0555 ^c	0.220 ± 0.0259 ^b	0.189 ± 0.0135 ^b	0.119 ± 0.0259 ^c	69.65	73.93	83.58
<i>Candida albicans</i>	0.896 ± 0.0325 ^{ef}	0.209 ± 0.0102 ^a	0.142 ± 0.0125 ^a	0.053 ± 0.0259 ^c	76.67	84.15	94.08
<i>Candida tropicalis</i>	0.679 ± 0.0102 ^b	0.198 ± 0.0325 ^c	0.159 ± 0.0325 ^c	0.065 ± 0.0102 ^a	70.83	76.58	90.42

Nil means that no ZOI had been measured.

^aAX Amoxicillin (antibacterial standard), ^{NS}Nystatin (antifungal standard), ^{ZOI}Zone of Inhibition, ^{MIC}Minimum Inhibitory Concentration.

Values are means ± SD (n = 3).

Data within the groups are analyzed using one-way analysis of variance (ANOVA) followed by ^{a, b, c, d, e, f, g, h}Duncan's multiple range test (DMRT).

penetration capabilities and different chemical effects concerning the relationship, metal NPs conjugation and interchange of the synthesized samples with biofilms [75]. It was seen that the synthesized MoS₂, the spinal ZnCo₂O₄, and Ag-decorated ZnCo₂O₄–MoS₂ nanocomposite hindered microbial development by more than 98%. It must be noted that the microbial cells cannot produce biofilm due to the control of exopolysaccharide, and microbial capsule formations [40].

4.6 Growth Curve Method

The influence of MoS₂, the spinal ZnCo₂O₄, and Ag-decorated ZnCo₂O₄–MoS₂ nanocomposite on *S. aureus* growth had presented in Fig. 13. *S. aureus* growth in the control sample happened quickly, with the most potent optical density at λ = 600 nm (OD₆₀₀) value having arrived at about 2.78 nm. After adding MoS₂ NPs, slight changes were detected, and OD₆₀₀ was calculated to be 1.87 nm. Indifference, the OD₆₀₀ value of ZnCo₂O₄ NPs (0.596 nm) was

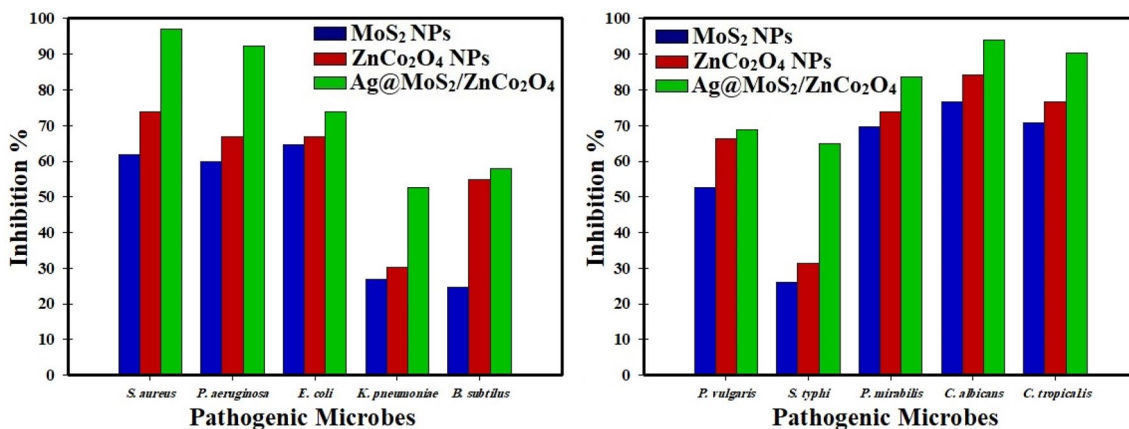


Fig. 12 Antibiofilm potential of MoS₂ NPs, the spinal ZnCo₂O₄ NPs, and Ag decorated MoS₂–ZnCo₂O₄ nanocomposite

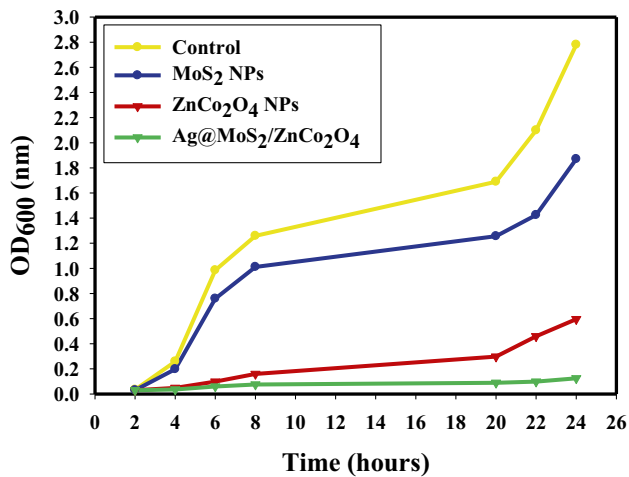


Fig. 13 The effect of MoS₂ NPs, the spinal ZnCo₂O₄ NPs, and Ag decorated MoS₂-ZnCo₂O₄ nanocomposite on the growth curve of *S. aureus*

lower than the control and MoS₂ NPs, while the value of Ag-decorated ZnCo₂O₄-MoS₂ nanocomposite showed the weakest results (0.125 nm), showing the repression impact on the growth of *S. aureus*. Silver-loaded MoS₂-ZnCo₂O₄ nanocomposite display further suppressing power rather than ZnCo₂O₄ NPs, and MoS₂ NPs that the unique synergistic effects may define, and the antibacterial activity of Ag NPs that described by various previous studies [29–32].

Typically, on the NPs surface, the photo-generation of reactive oxygen species (ROS) has been characterized by earlier reports [76]. Silver-loaded MoS₂-ZnCo₂O₄ nanocomposite creates ROS, inducing protein oxidation, DNA injury, and lipid peroxidation that can eliminate the bacteria without damaging the other cells. Moreover, *S. aureus* membrane maintains a negative charge, while the metal ion released from silver-loaded MoS₂-ZnCo₂O₄ nanocomposite (Ag⁺) possess a positive charge. So, they evolve in direct connection to crop to DNA replication, protein denaturation, and collapse of bacterial cells. The more increased hypersensitivity of the Gram-positive bacteria to the Ag NPs may be described due to the more inferior immobility of the bacterial cell membrane. A different probable causality can be the size, appearance, and surface charge of silver-loaded MoS₂-ZnCo₂O₄ nanocomposite, which could afford them more beneficial to connect with Gram-positive bacteria. Xu et al. [77], reported that NPs, behind UV-irradiation for 80 min, broke the *E. coli* membrane, suggesting that disinfection was completed. Different reports demonstrated that, most NPs, possessed antibacterial prospects toward other bacterial strains, like *S. aureus* and *E. coli* [29, 31].

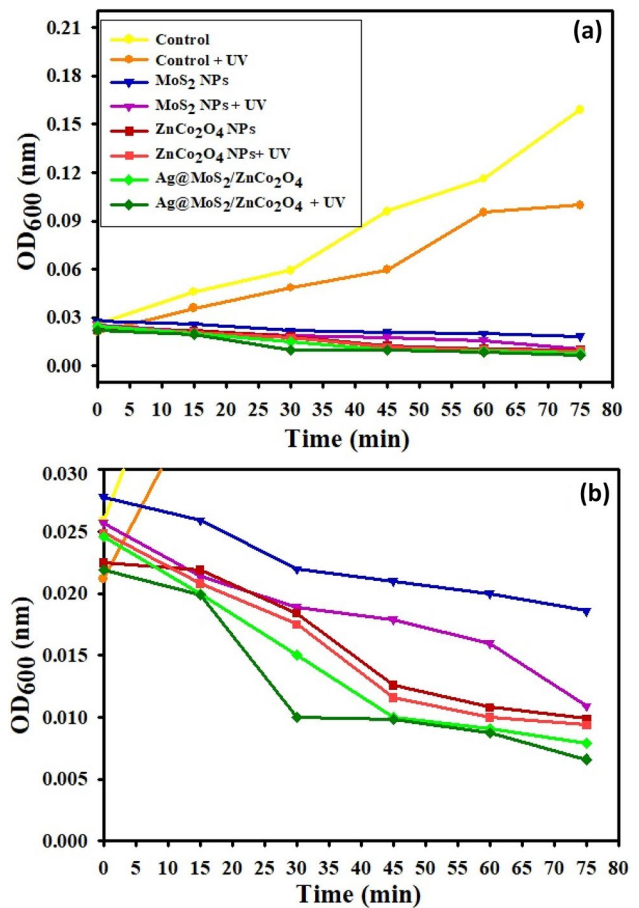


Fig. 14 a The UV effect on the antibacterial activity of MoS₂ NPs, the spinal ZnCo₂O₄ NPs, and Ag decorated MoS₂-ZnCo₂O₄ nanocomposite against *S. aureus*, and **b** zooming area of UV effect

4.7 UV Potential

Figure 14 shows that UV light is a promising deactivation of *S. aureus*, and the sensitivity is proportional to the exposure period. The positive influences regarding the attachment and growth of *S. aureus* had been noted across the display time (0 to 90 min with 15 min time intervals). The development of *S. aureus* was significantly hindered behind the treatment with silver-loaded MoS₂-ZnCo₂O₄ nanocomposite compared with the untreated control sample, MoS₂ NPs, and ZnCo₂O₄ NPs.

In UV experiment, the bacterial growth finished at the lowest growth because of the deactivation after UV illumination. UV rays was decided to increase the potential for photo-activation of silver-loaded MoS₂-ZnCo₂O₄ nanocomposite, and the prospect of silver-loaded MoS₂-ZnCo₂O₄ nanocomposite was more elevated than silver-free MoS₂ NPs, and ZnCo₂O₄ NPs. Silver-loaded MoS₂-ZnCo₂O₄ nanocomposite is an excellent disinfectant once it had excited by UV rays. NPs acquire photons, contribution in the

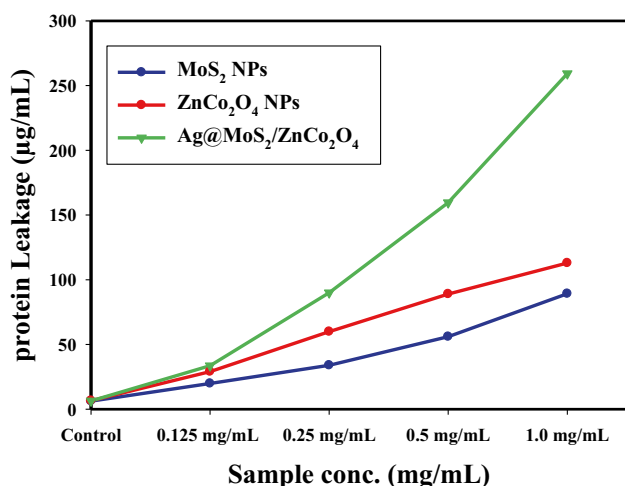


Fig. 15 The effect of MoS₂ NPs, the spinal ZnCo₂O₄ NPs, and Ag decorated MoS₂–ZnCo₂O₄ nanocomposite on the protein leakage from *S. aureus* cell membranes

formation of new ROS (O₂⁻, and H₂O₂), and active hydroxyl radical (·OH) in the existence of O₂ and H₂O (in air and/or water states) [78]. Microbial disinfection can be illustrated as ROS (H₂O₂) interacting with the membranes. After the penetration inside the microbes, active oxidative hydroxyl free radical was stable, and the effectual hindrance had been noted [76].

4.8 Bacterial Protein Leakage Investigation

In the treated *S. aureus* suspension, the amounts of proteins discharged were determined by the Bradford method. From Fig. 15, the amount of bacterial protein removed is directly proportional after increasing the concentration of MoS₂, the spinal ZnCo₂O₄, and Ag-decorated ZnCo₂O₄–MoS₂ nanocomposite (at different concentrations) and counted to be 89.20, 112.90, and 259.25 µg/mL following the treatment with MoS₂, the spinal ZnCo₂O₄, and Ag-decorated ZnCo₂O₄–MoS₂ nanocomposite (1.0 mg/mL), respectively which demonstrates the antibacterial features of the Ag-decorated ZnCo₂O₄–MoS₂ nanocomposite and describes the appearance of holes in the *S. aureus* membrane, which help in making the proteins bleed out from the *S. aureus* cytoplasm.

The presented results indicated that the synthesized Ag-decorated ZnCo₂O₄–MoS₂ nanocomposite enhanced the dissolving of *S. aureus* membrane and altering its permeability more than MoS₂ NPs, the spinal ZnCo₂O₄ NPs. The main cause for the repression of the bacterial growth is the positive effect of the metal against the bacterial membrane permeability which finally caused the protein leakage. Similar

articles such as [79] and [80] define the same results after the treating with NPs, which showed concentration-dependence for the dislodgement in the bacterial membrane and suggested leakage of bacterial intracellular organelles into the extracellular cell structure.

Paul et al. [81] demonstrated that the dissimilarity in membrane permeability of the bacteria was established in rate dissimilarity in connected electric conductivity. To determine the integrity of any microbes, the protein leakage assay is a critical method used for the determination. The leakage developed over time as standard microbial damage, and the leakage of cell constituents caused cell collapse.

4.9 SEM Reaction Mechanism

SEM analysis was directed to indicate the potential antimicrobial mechanism against *S. aureus*, as noted in Fig. 16. The SEM study regarding the control bacterial cells in the absence of Ag-decorated ZnCo₂O₄–MoS₂ nanocomposite (the most potent sample) presented bacterial groups typically prolonged and grown with a standard shape and count with the whole regular surface, as displayed in Fig. 16a and b.

After Ag-decorated ZnCo₂O₄–MoS₂ nanocomposite treatment, unusual morphological irregularities are identified in *S. aureus* (Fig. 16c), including the semi-lysis of the outer surface in some bacterial cells established by deformations of the *S. aureus* cells. On the other hand, the synthesized Ag decorated MoS₂–ZnCo₂O₄ nanocomposite performed the complete lysis of the bacterial cell and cell malformation, decreasing the total viable number (Fig. 16d) and creating holes on the surface of bacterial cells, and white layers are formed over the bacterial cells due to the chemisorption attractions between the active Ag-decorated ZnCo₂O₄–MoS₂ nanocomposite and the bacterial cell wall, which confirmed by the membrane leakage assay (Fig. 15).

The schematic diagram in Fig. 17 shows the possible antimicrobial mechanism. There were important and excellent potential actions such as reactive oxygen species (ROS) production due to the Ag loaded in the synthesized Ag-decorated ZnCo₂O₄–MoS₂ nanocomposite.

It is recommended that; the synthesized Ag-decorated ZnCo₂O₄–MoS₂ nanocomposite adhere to the microbial cells by chemisorption, and ROS will be developed, which could change the microbial morphology, reduce the microbial membrane permeability and provide the occupancy of oxidative stress genes about their replies because of the ROS production. We realize that Ag-decorated ZnCo₂O₄–MoS₂ nanocomposite begin their movement by bonding at the surface of the microbes, permitting membrane damage (as discussed in Fig. 17), construction of pits, and switching off the ions transportation activity. Then, the formation of ROS

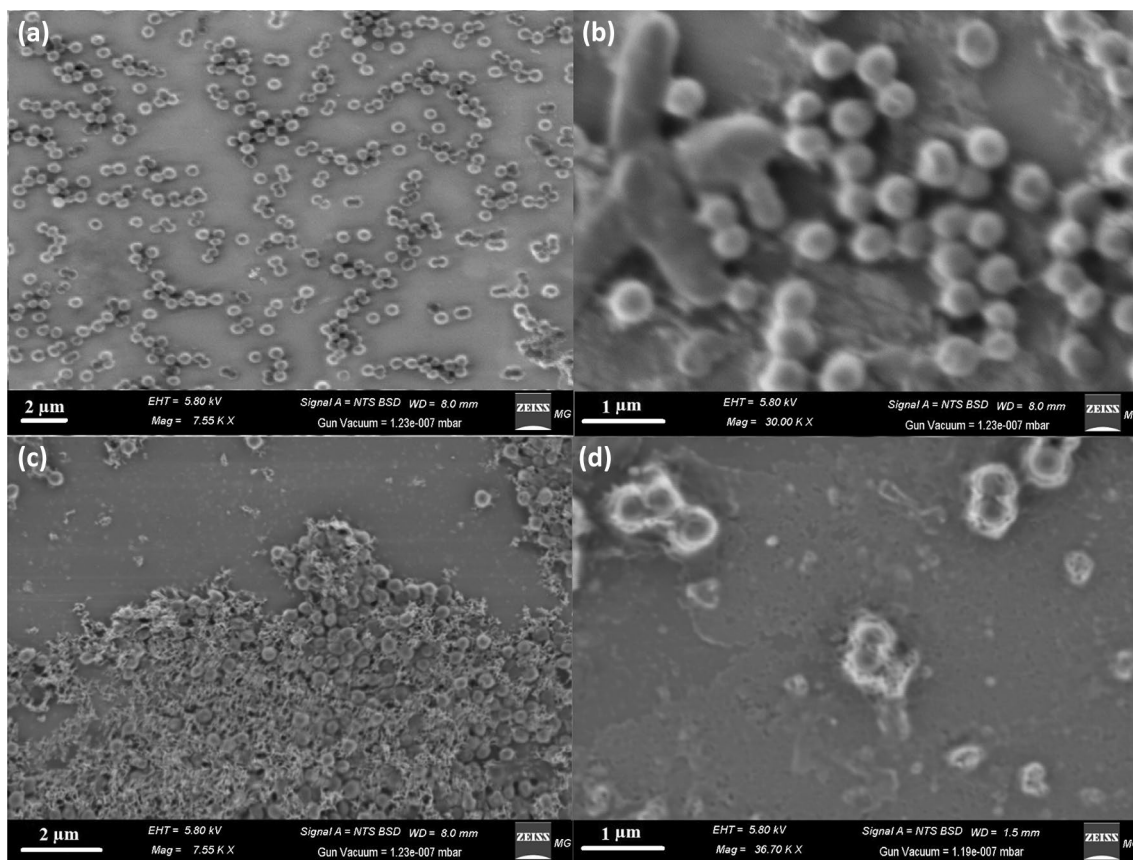


Fig. 16 Reaction mechanism determination using SEM analysis where **a, b** Control untreated *S. aureus*, and **c, d** Treated *S. aureus* with the most active synthesized sample (Ag decorated MoS_2 - ZnCo_2O_4 nanocomposite)

inside the microbial cells moved to the corresponding ions in the microbial cell, damaging all intracellular structures like DNA, plasmid, and various critical bacterial organelles. Now, cellular toxicity happens because of the oxidative stress created by ROS production [29, 30].

5 Conclusion

A Facile process was applied to synthesize Ag-decorated ZnCo_2O_4 - MoS_2 nanocomposite photocatalyst via gamma irradiation. The XRD and EDX results indicated the efficient fabrication and purity of the studied samples. Also, HR-TEM images confirmed the conjugation of Ag NPs with MoS_2 - ZnCo_2O_4 NPs. The photocatalyst shows enhanced, stable, and outstanding photocatalytic degradation towards MB 95.4% degradation of the dye at pH 12 was achieved after

180 min under light irradiation. The synthesized MoS_2 , the spinal ZnCo_2O_4 , and Ag-decorated ZnCo_2O_4 - MoS_2 nanocomposite samples had been tested for their antimicrobial potential upon selected pathogens (yeast and bacteria) throughout the agar-disc diffusion method. The tested samples display a positive potency to a wide spectrum of bacteria like *P. mirabilis*, *S. aureus*, *P. aeruginosa*, and *C. albicans*. In particular, Ag-decorated ZnCo_2O_4 - MoS_2 nanocomposite possessed the highest impact, followed by the spinal ZnCo_2O_4 NPs towards all the tested pathogenic microbes. In antibiofilm assay, the highest inhibition % of MoS_2 , the spinal ZnCo_2O_4 , and Ag-decorated ZnCo_2O_4 - MoS_2 nanocomposite percentage was documented for *S. aureus* (61.85%, 73.94%, and 97.06%), followed by *C. albicans* (76.67%, 84.15% and 94.08%), and *P. aureginosa* (59.84%, 66.79%, and 92.40%), respectively. In growth curve assay, *S. aureus* growth in the control sample happened quickly, with the most potent optical density at $\lambda = 600$ nm

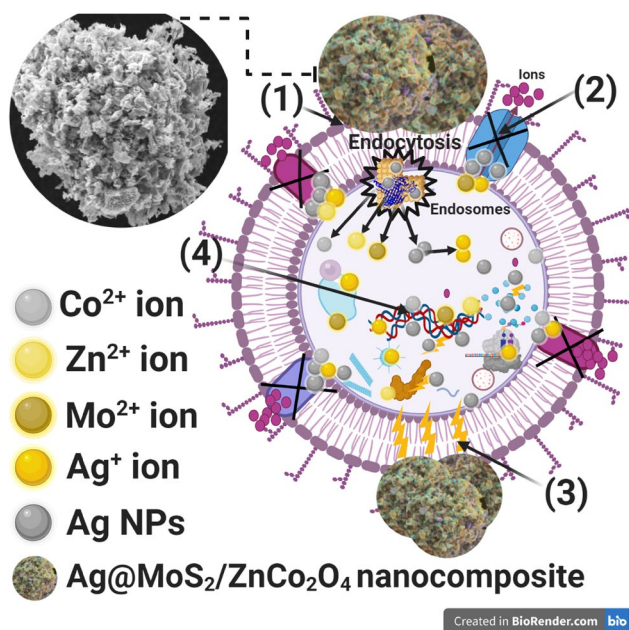


Fig. 17 Schematic indication about the four significant forms of the antibacterial possibility of Ag decorated $\text{MoS}_2\text{-ZnCo}_2\text{O}_4$ nanocomposite, where: 1. Ag decorated $\text{MoS}_2\text{-ZnCo}_2\text{O}_4$ nanocomposite attaches to the bacterial cell surface and results in membrane injury and limited transport movement. 2. Ag decorated $\text{MoS}_2\text{-ZnCo}_2\text{O}_4$ nanocomposite stop the ions transportation to and from the bacterial cell. 3. Ag decorated $\text{MoS}_2\text{-ZnCo}_2\text{O}_4$ nanocomposite develop and improve the ROS directing to bacterial cell wall crack. 4. Ag NPs liberated from Ag decorated $\text{MoS}_2\text{-ZnCo}_2\text{O}_4$ nanocomposite penetrate inside the bacterial cells and interact with cellular organelles, thereby influencing individual cellular machinery and modulating the cellular signal design and inducing cell end. Ag decorated $\text{MoS}_2\text{-ZnCo}_2\text{O}_4$ nanocomposite may serve as a vehicle to effectively deliver Ag^+ , Co^{2+} , Zn^{2+} , and Mo^{2+} ions to the bacterial cytoplasm and membrane, where proton motive force would reduce the pH to be less than 3.5 and enhance the liberation of ions

(OD_{600}) value having arrived at about 2.78 nm, while the value of Ag-decorated $\text{ZnCo}_2\text{O}_4\text{-MoS}_2$ nanocomposite showed the weakest results (0.125 nm), showing the repression impact on the growth of *S. aureus*. In UV experiment, the bacterial growth finished at the lowest growth because of the deactivation after UV illumination. In protein leakage assay, the amount of bacterial protein removed is directly proportional after increasing the concentration of MoS_2 , the spinal ZnCo_2O_4 , and Ag-decorated $\text{ZnCo}_2\text{O}_4\text{-MoS}_2$ nanocomposite (at different concentrations) and counted to be 89.20, 112.90, and 259.25 $\mu\text{g}/\text{ml}$ following the treatment with MoS_2 , the spinal ZnCo_2O_4 , and Ag-decorated $\text{ZnCo}_2\text{O}_4\text{-MoS}_2$ nanocomposite, respectively (1.0 mg/mL). SEM imaging reaction mechanism illustrated that, after Ag-decorated $\text{ZnCo}_2\text{O}_4\text{-MoS}_2$ treatment, unusual morphological irregularities are identified in *S. aureus*, including the semi-lysis of the outer surface in some bacterial cells established by deformations of the *S. aureus* cells.

Supplementary Information The online version contains supplementary material available at <https://doi.org/10.1007/s10904-022-02387-w>.

Funding Open access funding provided by The Science, Technology & Innovation Funding Authority (STDF) in cooperation with The Egyptian Knowledge Bank (EKB). None.

Data Availability Not applicable.

Declarations

Conflict of interest The authors declare that they have no conflict of interest.

Ethical Approval Not required.

Consent to Participate Not applicable.

Consent to Publish Not applicable.

Open Access This article is licensed under a Creative Commons Attribution 4.0 International License, which permits use, sharing, adaptation, distribution and reproduction in any medium or format, as long as you give appropriate credit to the original author(s) and the source, provide a link to the Creative Commons licence, and indicate if changes were made. The images or other third party material in this article are included in the article's Creative Commons licence, unless indicated otherwise in a credit line to the material. If material is not included in the article's Creative Commons licence and your intended use is not permitted by statutory regulation or exceeds the permitted use, you will need to obtain permission directly from the copyright holder. To view a copy of this licence, visit <http://creativecommons.org/licenses/by/4.0/>.

References

1. X. Zou, J. Zhang, X. Zhao, Z. Zhang, MoS_2/RGO composites for photocatalytic degradation of ranitidine and elimination of NDMA formation potential under visible light. *Chem. Eng. J.* **383**, 123084 (2020)
2. L. Shi, W. Ding, S. Yang, Z. He, S. Liu, Rationally designed $\text{MoS}_2/\text{protonated g-C}_3\text{N}_4$ nanosheet composites as photocatalysts with an excellent synergistic effect toward photocatalytic degradation of organic pollutants. *J. Hazard. Mater.* **347**, 431–441 (2018)
3. Y. Fu, L. Qin, D. Huang, G. Zeng, C. Lai, B. Li, J. He, H. Yi, M. Zhang, M. Cheng, X. Wen, Chitosan functionalized activated coke for Au nanoparticles anchoring: green synthesis and catalytic activities in hydrogenation of nitrophenols and azo dyes. *Appl. Catal. B* **255**, 117740 (2019)
4. A.İ. Vaizogullar, Ternary $\text{CdS}/\text{MoS}_2/\text{ZnO}$ photocatalyst: synthesis, characterization and degradation of ofloxacin under visible light irradiation. *J. Inorg. Organomet. Polym. Mater.* **30**(10), 4129–4141 (2020)
5. Y. Fan, Y.-N. Yang, C. Ding, Preparation of $\text{g-C}_3\text{N}_4/\text{MoS}_2$ composite material and its visible light catalytic performance. *J. Inorg. Organomet. Polym. Mater.* **31**(12), 4722–4730 (2021)
6. Y. Cao, Q. Li, W. Wang, Construction of a crossed-layer-structure $\text{MoS}_2/\text{g-C}_3\text{N}_4$ heterojunction with enhanced photocatalytic performance. *RSC Adv.* **7**(10), 6131–6139 (2017)
7. S. Bai, L. Wang, X. Chen, J. Du, Y. Xiong, Chemically exfoliated metallic MoS_2 nanosheets: a promising supporting

- co-catalyst for enhancing the photocatalytic performance of TiO₂ nanocrystals. *Nano Res.* **8**(1), 175–183 (2015)
8. Y. Fu, Z. Ren, J. Wu, Y. Li, W. Liu, P. Li, L. Xing, J. Ma, H. Wang, X. Xue, Direct Z-scheme heterojunction of ZnO/MoS₂ nanoarrays realized by flowing-induced piezoelectric field for enhanced sunlight photocatalytic performances. *Appl. Catal. B* **285**, 119785 (2021)
 9. P. Feng, Y. Kong, L. Yu, Y. Li, C. Gao, S. Peng, H. Pan, Z. Zhao, C. Shuai, Molybdenum disulfide nanosheets embedded with nanodiamond particles: co-dispersion nanostructures as reinforcements for polymer scaffolds. *Appl. Mater. Today* **17**, 216–226 (2019)
 10. W. Huang, Y. Li, Q. Fu, M. Chen, Fabrication of a novel biochar decorated nano-flower-like MoS₂ nanomaterial for the enhanced photodegradation activity of ciprofloxacin: performance and mechanism. *Mater. Res. Bull.* **147**, 111650 (2022)
 11. A. Sathiyapriya, D. Geetha, K. Karthik, M. Rajamoorthy, Investigations on the enhanced photocatalytic activity of (Ag, La) substituted nickel cobaltite spinels. *Solid State Sci.* **98**, 105992 (2019)
 12. M.H. Habibi, P. Bagheri, Enhanced photo-catalytic degradation of naphthol blue black on nano-structure MnCo₂O₄: charge separation of the photo-generated electron-hole pair. *J. Mater. Sci.* **28**(1), 289–294 (2017)
 13. R. Hassandoost, A. Kotb, Z. Movafagh, M. Esmat, R. Guegan, S. Endo, W. Jevasuwan, N. Fukata, Y. Sugahara, A. Khataee, Y. Yamauchi, Y. Ide, E. Doustkhah, Nanoarchitecturing bimetallic manganese cobaltite spinels for sonocatalytic degradation of oxy-tetracycline. *Chem. Eng. J.* **431**, 133851 (2022)
 14. S.B. Kokane, S.R. Suryawanshi, R. Sasikala, M.A. More, S.D. Sartale, Architecture of 3D ZnCo₂O₄ marigold flowers: influence of annealing on cold emission and photocatalytic behavior. *Mater. Chem. Phys.* **194**, 55–64 (2017)
 15. J. Rashid, M.A. Barakat, R.M. Mohamed, I.A. Ibrahim, Enhancement of photocatalytic activity of zinc/cobalt spinel oxides by doping with ZrO₂ for visible light photocatalytic degradation of 2-chlorophenol in wastewater. *J. Photochem. Photobiol. A* **284**, 1–7 (2014)
 16. R. Behnood, G. Sodeifian, Novel ZnCo₂O₄ embedded with S, N-CQDs as efficient visible-light photocatalyst. *J. Photochem. Photobiol. A* **405**, 112971 (2021)
 17. S.A. Heidari-Asil, S. Zinatloo-Ajabshir, H.A. Alshamsi, A. Al-Nayili, Q.A. Yousif, M. Salavati-Niasari, Magnetically recyclable ZnCo₂O₄/Co₃O₄ nano-photocatalyst: green combustion preparation, characterization and its application for enhanced degradation of contaminated water under sunlight. *Int. J. Hydrog. Energy* **47**(38), 16852–16861 (2022)
 18. G.F. Teixeira, E. Silva Junior, R. Vilela, M.A. Zaghete, F. Colmati, Perovskite structure associated with precious metals: influence on heterogeneous catalytic process. *Catalysts* **9**(9), 721 (2019)
 19. J. Singh, K. Sahu, S. Mohapatra, Ion beam engineering of morphological, structural, optical and photocatalytic properties of Ag-TiO₂-PVA nanocomposite thin film. *Ceram. Int.* **45**(6), 7976–7983 (2019)
 20. J. Singh, K. Sahu, A. Pandey, M. Kumar, T. Ghosh, B. Satpati, T. Som, S. Varma, D. Avasthi, S. Mohapatra, Atom beam sputtered Ag-TiO₂ plasmonic nanocomposite thin films for photocatalytic applications. *Appl. Surf. Sci.* **411**, 347–354 (2017)
 21. W. Zhang, Y. Ma, X. Zhu, S. Liu, T. An, J. Bao, X. Hu, H. Tian, Fabrication of Ag decorated g-C₃N₄/LaFeO₃ Z-scheme heterojunction as highly efficient visible-light photocatalyst for degradation of methylene blue and tetracycline hydrochloride. *J. Alloy Compd.* **864**, 158914 (2021)
 22. Y. Jia, H. Ma, C. Liu, Au nanoparticles enhanced Z-scheme Au-CoFe₂O₄/MoS₂ visible light photocatalyst with magnetic retrievability. *Appl. Surf. Sci.* **463**, 854–862 (2019)
 23. J. Fu, S. Cao, J. Yu, Dual Z-scheme charge transfer in TiO₂-Ag-Cu₂O composite for enhanced photocatalytic hydrogen generation. *J. Materiomics* **1**(2), 124–133 (2015)
 24. A. Khezerlou, M. Alizadeh-sani, M. Azizi-lalabadi, A. Ehsani, Microbial Pathogenesis Nanoparticles and their antimicrobial properties against pathogens including bacteria, fungi, parasites and viruses. *Microb. Pathogen.* **123**, 505–526 (2018)
 25. P. Feng, Y. Kong, M. Liu, S. Peng, C. Shuai, Dispersion strategies for low-dimensional nanomaterials and their application in biopolymer implants. *Mater. Today Nano* **15**, 100127 (2021)
 26. C. Shuai, W. Guo, P. Wu, W. Yang, S. Hu, Y. Xia, P. Feng, A graphene oxide-Ag co-dispersing nanosystem: dual synergistic effects on antibacterial activities and mechanical properties of polymer scaffolds. *Chem. Eng. J.* **347**, 322–333 (2018)
 27. L. Wang, C. Hu, L. Shao, The antimicrobial activity of nanoparticles: present situation and prospects for the future. *Int. J. Nanomed.* **12**, 1227 (2017)
 28. S. Murthy, P. Effiong, C.C. Fei, *Metal Oxide Nanoparticles in Biomedical Applications, Metal Oxide Powder Technologies* (Elsevier, Amsterdam, 2020), pp. 233–251
 29. M.I.A. Abdel Maksoud, M.M. Ghobashy, G.S. El-Sayyad, A.M. El-Khawaga, M.A. Elsayed, A.H. Ashour, Gamma irradiation-assisted synthesis of PANi/Ag/MoS₂/LiCo_{0.5}Fe₂O₄ nanocomposite: efficiency evaluation of photocatalytic bisphenol A degradation and microbial decontamination from wastewater. *Opt. Mater.* **119**, 111396 (2021)
 30. M.I.A. Abdel Maksoud, G.S. El-Sayyad, H.S. El-Bastawisy, R.M. Fathy, Antibacterial and antibiofilm activities of silver-decorated zinc ferrite nanoparticles synthesized by a gamma irradiation-coupled sol-gel method against some pathogenic bacteria from medical operating room surfaces. *RSC Adv.* **11**(45), 28361–28374 (2021)
 31. M.I.A. Abdel Maksoud, G.S. El-Sayyad, E. Fayad, A. Alyamani, O.A. Abu Ali, A.A. Elshamy, Gamma irradiation assisted the sol-gel method for silver modified-nickel molybdate nanoparticles synthesis: unveiling the antimicrobial, and antibiofilm activities against some pathogenic microbes. *J. Inorg. Organomet. Polym. Mater.* **32**(2), 728–740 (2022)
 32. E.A. Mustafa, A.E.G. Hashem, H.N. Elhifnawi, H.G. Nada, R.A. Khattab, One-pot biosynthesis of silver nanoparticles with potential antimicrobial and antibiofilm efficiency against otitis media-causing pathogens. *Eur. J. Clin. Microbiol. Infect. Dis.* **40**(1), 49–58 (2021)
 33. A. Baraka, S. Dickson, M. Gobara, G.S. El-Sayyad, M. Zorainy, M.I. Awaad, H. Hatem, M.M. Kotb, A.F. Tawfic, Synthesis of silver nanoparticles using natural pigments extracted from Alfalfa leaves and its use for antimicrobial activity. *Chem. Pap.* **71**(11), 2271–2281 (2017)
 34. G.G. Flores-Rojas, F. López-Saucedo, E. Bucio, Gamma-irradiation applied in the synthesis of metallic and organic nanoparticles: a short review. *Radiat. Phys. Chem.* **169**, 107962 (2020)
 35. M.I.A. Abdel Maksoud, A. El-Ghandour, G.S. El-Sayyad, R.A. Fahim, A.H. El-Hanbaly, M. Bekhit, E.K. Abdel-Khalek, H.H. El-Bahnasawy, M. Abd Elkodous, A.H. Ashour, A.S. Awed, Unveiling the effect of Zn²⁺ substitution in enrichment of structural, magnetic, and dielectric properties of cobalt ferrite. *J. Inorg. Organomet. Polym. Mater.* **30**(9), 3709–3721 (2020)
 36. M.T. Yagub, T.K. Sen, H.M. Ang, Equilibrium, kinetics, and thermodynamics of methylene blue adsorption by pine tree leaves. *Water Air Soil Pollut.* **223**(8), 5267–5282 (2012)
 37. H.G. Nada, R. Mohsen, M.E. Zaki, A.A. Aly, Evaluation of chemical composition, antioxidant, antibiofilm and antibacterial potency of essential oil extracted from gamma irradiated clove (*Eugenia caryophyllata*) buds. *J. Food Meas. Charact.* **16**(1), 673–686 (2022)

38. R.M. Fathy, A.Y. Mahfouz, Eco-friendly graphene oxide-based magnesium oxide nanocomposite synthesis using fungal fermented by-products and gamma rays for outstanding antimicrobial, antioxidant, and anticancer activities. *J. Nanostruct. Chem.* **11**(2), 301–321 (2021)
39. G.D. Christensen, W.A. Simpson, A.L. Bisno, E.H. Beachey, Adherence of slime-producing strains of *Staphylococcus epidermidis* to smooth surfaces. *Infect. Immun.* **37**(1), 318–326 (1982)
40. M.A. Ansari, H.M. Khan, A.A. Khan, S.S. Cameotra, R. Pal, Antibiofilm efficacy of silver nanoparticles against biofilm of extended spectrum β -lactamase isolates of *Escherichia coli* and *Klebsiella pneumoniae*. *Appl. Nanosci.* **4**(7), 859–868 (2014)
41. W. Huang, J.-Q. Wang, H.-Y. Song, Q. Zhang, G.-F. Liu, Chemical analysis and in vitro antimicrobial effects and mechanism of action of *Trachyspermum coticum* essential oil against *Escherichia coli*. *Asian Pac. J. Trop. Med.* **10**(7), 663–669 (2017)
42. M. Abd Elkodous, G.S. El-Sayyad, S.M. Youssry, H.G. Nada, M. Gobara, M.A. Elsayed, A.M. El-Khawaga, G. Kawamura, W.K. Tan, A.I. El-Batal, Carbon-dot-loaded $\text{Co}_x\text{Ni}_{1-x}\text{Fe}_2\text{O}_4$; $x = 09/\text{SiO}_2/\text{TiO}_2$ nanocomposite with enhanced photocatalytic and antimicrobial potential: an engineered nanocomposite for wastewater treatment. *Sci. Rep.* **10**(1), 1–22 (2020)
43. H. Agarwal, A. Nakara, S. Menon, V. Shanmugam, Eco-friendly synthesis of zinc oxide nanoparticles using *Cinnamomum Tamala* leaf extract and its promising effect towards the antibacterial activity. *J. Drug Deliv. Sci. Technol.* **53**, 101212 (2019)
44. A.M. Brown, A new software for carrying out one-way ANOVA post hoc tests. *Comput. Methods Prog. Biomed.* **79**(1), 89–95 (2005)
45. L. Wang, D. Li, J. Zhang, C. Song, H. Xin, X. Qin, Porous flower-like ZnCo_2O_4 and $\text{ZnCo}_2\text{O}_4/\text{C}$ composite: a facile controllable synthesis and enhanced electrochemical performance. *Ionics* **26**(9), 4479–4487 (2020)
46. Y. Qi, N. Wang, Q. Xu, H. Li, P. Zhou, X. Lu, G. Zhao, A green route to fabricate MoS_2 nanosheets in water–ethanol– CO_2 . *Chem. Commun.* **51**(31), 6726–6729 (2015)
47. S. Sathiyar, H. Ahmad, W. Chong, S. Lee, S. Sivabalan, Evolution of the polarizing effect of MoS_2 . *IEEE Photonics J.* **7**(6), 1–10 (2015)
48. Y. Liu, Y. Zhao, L. Jiao, J. Chen, A graphene-like MoS_2 /graphene nanocomposite as a highperformance anode for lithium ion batteries. *J. Mater. Chem. A* **2**(32), 13109–13115 (2014)
49. F.A. Monikh, M.G. Vijver, Z. Guo, P. Zhang, G.K. Darbha, W.J. Peijnenburg, Metal sorption onto nanoscale plastic debris and trojan horse effects in daphnia magna: role of dissolved organic matter. *Water Res.* **186**, 116410 (2020)
50. Z. Wang, J.-J. Han, N. Zhang, D.-D. Sun, T. Han, Synthesis of polyaniline/graphene composite and its application in zinc-rechargeable batteries. *J. Solid State Electrochem.* **23**(12), 3373–3382 (2019)
51. M. Tamboli, M. Kulkarni, S. Deshmukh, B. Kale, Synthesis and spectroscopic characterisation of silver–polyaniline nanocomposite. *Mater. Res. Innov.* **17**(2), 112–116 (2013)
52. S.P. Deshmukh, A.G. Dhodamani, S.M. Patil, S.B. Mullani, K.V. More, S.D. Delekar, Interfacially interactive ternary silver-supported polyaniline/multiwalled carbon nanotube nanocomposites for catalytic and antibacterial activity. *ACS Omega* **5**(1), 219–227 (2019)
53. P. Debye, P. Scherrer, Interference of irregularly oriented particles in x-rays. *Phys. Ziet* **17**, 277–283 (1916)
54. J.-Y. Wu, M.-N. Lin, L.-D. Wang, T. Zhang, Photoluminescence of MoS_2 prepared by effective grinding-assisted sonication exfoliation. *J. Nanomater.* (2014)
55. B. Alshahrani, H.I. ElSaeedy, S. Fares, A.H. Korna, H.A. Yakout, M.I.A.A. Maksoud, R.A. Fahim, M. Gobara, A.H. Ashour, The effect of Ce^{3+} doping on structural, optical, ferromagnetic resonance, and magnetic properties of ZnFe_2O_4 nanoparticles. *J. Mater. Sci.* **32**(1), 780–797 (2021)
56. J. Tauc, R. Grigorovici, A. Vancu, Optical properties and electronic structure of amorphous germanium. *Phys. Status Solidi B* **15**(2), 627–637 (1966)
57. M.H. Khedr, M. Bahgat, W.M.A.E. Roubay, Synthesis, magnetic properties and photocatalytic activity of $\text{CuFe}_2\text{O}_4/\text{MgFe}_2\text{O}_4$ and $\text{MgFe}_2\text{O}_4/\text{CuFe}_2\text{O}_4$ core/shell nanoparticles. *Mater. Technol.* **23**(1), 27–32 (2008)
58. S. Su, C. Cao, Y. Zhao, D.D. Dionysiou, Efficient transformation and elimination of roxarsone and its metabolites by a new $\alpha\text{-FeOOH}/\text{GCA}$ activating persulfate system under UV irradiation with subsequent As(V) recovery. *Appl. Catal. B* **245**, 207–219 (2019)
59. S.B. Hammouda, F. Zhao, Z. Safaei, D.L. Ramasamy, B. Doshi, M. Sillanpää, Sulfate radical-mediated degradation and mineralization of bisphenol F in neutral medium by the novel magnetic $\text{Sr}_2\text{CoFeO}_6$ double perovskite oxide catalyzed peroxyoxosulfate: Influence of co-existing chemicals and UV irradiation. *Appl. Catal. B* **233**, 99–111 (2018)
60. K.M. Reza, A.S.W. Kurny, F. Gulshan, Parameters affecting the photocatalytic degradation of dyes using TiO_2 : a review. *Appl Water Sci* **7**(4), 1569–1578 (2017)
61. M. Hao, Y. Li, L. Gao, C. Ji, R. Qu, Z. Yang, C. Sun, Y. Zhang, In-situ hard template synthesis of mesoporous carbon/graphite carbon nitride (C/CN-T-x) composites with high photocatalytic activities under visible light irradiation. *Solid State Sci.* **109**, 106428 (2020)
62. R.G. Chaudhary, A.K. Potbhare, S.K.T. Aziz, M.S. Umekar, S.S. Bhuyar, A. Mondal, Phytochemically fabricated reduced graphene oxide-ZnO NCs by *Sesbania bispinosa* for photocatalytic performances. *Mater. Today* **36**, 756–762 (2021)
63. Z. Li, H. Hanafy, L. Zhang, L. Sellaoui, M. Schadeck Netto, M.L.S. Oliveira, M.K. Seliem, G. Luiz Dotto, A. Bonilla-Petriciolet, Q. Li, Adsorption of congo red and methylene blue dyes on an ashitaba waste and a walnut shell-based activated carbon from aqueous solutions: experiments, characterization and physical interpretations. *Chem. Eng. J.* **388**, 124263 (2020)
64. B.-M. Jun, S.S. Elanchezhian, Y. Yoon, D. Wang, S. Kim, S. Muthu Prabhu, C.M. Park, Accelerated photocatalytic degradation of organic pollutants over carbonate-rich lanthanum-substituted zinc spinel ferrite assembled reduced graphene oxide by ultraviolet (UV)-activated persulfate. *Chem. Eng. J.* **393**, 124733 (2020)
65. W.M.A. El Roubay, Selective adsorption and degradation of organic pollutants over Au decorated Co doped titanate nanotubes under simulated solar light irradiation. *J. Taiwan Inst. Chem. Eng.* **88**, 201–214 (2018)
66. H. Nawaz, M. Umar, I. Nawaz, Q. Zia, M. Tabassum, H. Razzaq, H. Gong, X. Zhao, X. Liu, Photodegradation of textile pollutants by nanocomposite membranes of polyvinylidene fluoride integrated with polyaniline–titanium dioxide nanotubes. *Chem. Eng. J.* **419**, 129542 (2021)
67. S. Banerjee, M.C. Chattopadhyaya, Adsorption characteristics for the removal of a toxic dye, tartrazine from aqueous solutions by a low cost agricultural by-product. *Arab. J. Chem.* **10**, S1629–S1638 (2017)
68. Y. Miyah, A. Lahrichi, M. Idrissi, S. Boujraf, H. Taouda, F. Zerrouq, Assessment of adsorption kinetics for removal potential of Crystal Violet dye from aqueous solutions using Moroccan

- pyrophyllite. *J. Assoc. Arab Univ. Basic Appl. Sci.* **23**, 20–28 (2017)
69. H. Zhang, D. Liu, S. Ren, H. Zhang, Kinetic studies of direct blue photodegradation over flower-like TiO_2 . *Res. Chem. Intermed.* **43**(3), 1529–1542 (2017)
70. T. Jin, Y. He, Antibacterial activities of magnesium oxide (MgO) nanoparticles against foodborne pathogens. *J. Nanopart. Res.* **13**(12), 6877–6885 (2011)
71. K. Karthik, M.M. Naik, M. Shashank, M. Vinuth, V. Revathi, Microwave-assisted ZrO_2 nanoparticles and its photocatalytic and antibacterial studies. *J. Clust. Sci.* **30**(2), 311–318 (2019)
72. K. Karthik, S. Dhanuskodi, C. Gobinath, S. Prabukumar, S. Sivaramakrishnan, Fabrication of MgO nanostructures and its efficient photocatalytic, antibacterial and anticancer performance. *J. Photochem. Photobiol. B* **190**, 8–20 (2019)
73. Z.-X. Tang, B.-F. Lv, MgO nanoparticles as antibacterial agent: preparation and activity. *Braz. J. Chem. Eng.* **31**(3), 591–601 (2014)
74. C. Ashajyothi, K.H. Harish, N. Dubey, R.K. Chandrakanth, Antibiofilm activity of biogenic copper and zinc oxide nanoparticles-antimicrobials collegiate against multiple drug resistant bacteria: a nanoscale approach. *J. Nanostruct. Chem.* **6**(4), 329–341 (2016)
75. H.-J. Park, H.Y. Kim, S. Cha, C.H. Ahn, J. Roh, S. Park, S. Kim, K. Choi, J. Yi, Y. Kim, Removal characteristics of engineered nanoparticles by activated sludge. *Chemosphere* **92**(5), 524–528 (2013)
76. A. Joe, S.-H. Park, D.-J. Kim, Y.-J. Lee, K.-H. Jhee, Y. Sohn, E.-S. Jang, Antimicrobial activity of ZnO nanoplates and its Ag nanocomposites: insight into an ROS-mediated antibacterial mechanism under UV light. *J. Solid State Chem.* **267**, 124–133 (2018)
77. Y. Xu, Q. Liu, M. Xie, S. Huang, M. He, L. Huang, H. Xu, H. Li, Synthesis of zinc ferrite/silver iodide composite with enhanced photocatalytic antibacterial and pollutant degradation ability. *J. Colloid Interface Sci.* **528**, 70–81 (2018)
78. L.F. Gaunt, C.B. Beggs, G.E. Georghiou, Bactericidal action of the reactive species produced by gas-discharge nonthermal plasma at atmospheric pressure: a review. *IEEE Trans. Plasma Sci.* **34**(4), 1257–1269 (2006)
79. S. Rajesh, V. Dharanishanthi, A.V. Kanna, Antibacterial mechanism of biogenic silver nanoparticles of *Lactobacillus acidophilus*. *J. Exp. Nanosci.* **10**(15), 1143–1152 (2015)
80. Z. Azam, A. Ayaz, M. Younas, Z. Qureshi, B. Arshad, W. Zaman, F. Ullah, M.Q. Nasar, S. Bahadur, M.M. Irfan, Microbial synthesized cadmium oxide nanoparticles induce oxidative stress and protein leakage in bacterial cells. *Microb. Pathog.* **144**, 104188 (2020)
81. D. Paul, S. Maiti, D.P. Sethi, S. Neogi, Bi-functional NiO-ZnO nanocomposite: synthesis, characterization, antibacterial and photo assisted degradation study. *Adv. Powder Technol.* **32**(1), 131–143 (2021)

Publisher's Note Springer Nature remains neutral with regard to jurisdictional claims in published maps and institutional affiliations.